

NUCLEATION, GROWTH AND STRAIN RELIEF IN COPPER HETEROEPITAXY ON NICKEL(100)

THÈSE N° 1607 (1996)

PRÉSENTÉE AU DÉPARTEMENT DE PHYSIQUE

ÉCOLE POLYTECHNIQUE FÉDÉRALE DE LAUSANNE

POUR L'OBTENTION DU GRADE DE DOCTEUR ÈS SCIENCES

PAR

Lorenz P. NEDELMANN

Dipl. Ing. Chemie, Technische Hochschule Darmstadt, Allemagne
de nationalité allemande

acceptée sur proposition du jury:

Prof. K. Kern, directeur de thèse
Dr C. Boragno, corapporteur
Dr R. Gotthardt, corapporteur
Dr J. Wolschläger, corapporteur

Lausanne, EPFL
1997

To Déborah

Vous m'expliquez ce monde avec une image ...

Resumé

Nous rapportons une étude des processus microscopiques intervenants dans la croissance hétéroépitaxiale des métaux à l'aide de la microscopie à effet tunnel (STM) à température variable et par diffraction d'électrons de basse énergie à haute résolution (SPA-LEED). De nombreuses mesures effectuées sur une large gamme de températures ont permis une étude détaillée de la cinétique du cuivre, déposé par jet moléculaire, sur la surface (100) du nickel. Le processus de nucléation a été caractérisé à partir des densités de saturation des îlots, obtenues en variant de manière systématique le taux de déposition et de la température du substrat. Les grandeurs microscopiques telles que l'énergie de diffusion des monomères sur une terrasse et l'énergie de liaison des dimères supportés ont été évaluées dans le cadre de la théorie de nucléation en champ moyen. La symétrie quadratique du substrat explique que la taille minimale des îlots stables saute directement du dimère au tetramère.

Dans les conditions standards, la diffusion est largement supérieure au taux de déposition et le processus de croissance est suffisamment rapide pour avoir lieu lors même de la déposition (croissance dynamique). Lorsque le rapport diffusion/taux de déposition est suffisamment petit, la croissance se poursuit bien au-delà de la déposition. La distribution normalisée de la taille des îlots correspond alors à celle caractéristique d'une croissance statistique pour laquelle le monomère est l'îlot stable de taille minimale.

Ce comportement a été reproduit quantitativement à l'aide de "rate equations" utilisant les énergies de diffusion et de liaison tirées de l'expérience.

Le système Cu/Ni(100) permet d'étudier l'effet des contraintes de "mismatch" sur la croissance: les paramètres de maille du cuivre et du nickel diffèrent de 2.6 %. Nous avons constaté que la morphologie des îlots traduit l'influence du "mismatch" même pour des taux de recouvrements infimes (0.03 monocouches): les îlots d'une taille supérieure à 500 atomes sont ramifiés, alors que dans le cas de réseaux quadratiques, on ne s'attendrait à trouver des îlots non-compacts qu'à extrêmement basses températures et hors des conditions d'équilibre thermodynamique. Nous démontrerons que ces formes ramifiées correspondent bel et bien à une forme d'équilibre puisqu'elles permettent une relaxation optimale de la contrainte de mismatch sur le pourtour des îlots.

La croissance de plusieurs monocouches a révélé un nouveau mécanisme de relaxation des contraintes: déjà lors de la formation de la première monocouche, des chaînes monoatomiques de cuivre sont expulsées de la position d'équilibre (hollow) pour se retrouver dans une position de diffusion (bridge), ce qui augmente leur distance d'avec le substrat. Cette relaxation donne lieu à une structure en franges qui se détachent en relief de la surface. Pour chaque couche de cuivre supplémentaire, les franges s'élargissent d'un atome ce qui donne naissance à des interfaces internes de type {111}.

Ce type de croissance diffère des prédictions de la théorie continue, pourtant communément acceptée, qui prédit une croissance de type pseudomorphe jusqu'à des épaisseurs de ~ 8 monocouches.

Le Cu/Ni(100) croît couche-par-couche et, à partir de 2 monocouches, par adhésion aux marches. Les spectres de diffractions ne présentent dès lors pas les complications dues au pourtour des îlots. Ce système permet donc de confronter de manière idéale les mesures STM et SPA-LEED, deux instruments parmi les plus puissants pour l'étude des surfaces. Ce travail met en valeur les avantages et les inconvénients de chacune de ces deux méthodes.

Abstract

By means of variable temperature scanning tunneling microscopy (STM) and spot profile analysis of low energy electron diffraction (SPA-LEED), microscopic processes in heteroepitaxial metal growth have been studied. The model system chosen is copper on Ni(100) grown by molecular beam epitaxy; the ability to access a wide range of temperatures permits to study the kinetic aspects in detail.

In order to characterize the nucleation behaviour, the external parameters deposition flux and temperature have been systematically varied and the resulting saturation island density analysed. The use of mean-field nucleation theory allowed to determine microscopic quantities such as the activation energy of monomer terrace diffusion or the dimer binding energy. The square symmetry of the substrate is responsible for a direct transition of the smallest stable island from dimer to tetramer occurring at 320 K.

Usually growth processes are sufficiently fast to take place simultaneously with deposition (dynamic growth regime). For low ratios diffusion constant flux a growth regime has been characterized where significant parts of the growth processes occur after deposition. In this growth regime, the island density becomes almost independent of substrate temperature and flux, and the scaled island size distribution closely resembles that of statistic growth, where the monomer is the smallest stable island. This regime is quantitatively simulated by a rate equation analysis employing the aforementioned microscopic parameters.

Copper on Ni(100) is well-suited to study the effects of compressive strain in heteroepitaxial growth; the lattice mismatch is 2.6 %. Already at very low coverages (0.03 monolayers), we found strain related growth

morphologies. Islands larger than 500 atoms are ramified. This is surprising, as for a square lattice non-compact growth forms are expected only at extremely low temperatures far away from equilibrium. The ramified island shapes are demonstrated to be equilibrium forms and to render the strain relief at step edges more efficient.

The study of the multilayer growth revealed a novel strain relief mechanism. In the first monolayer, monatomic chains of copper atoms are shifted from hollow to bridge sites and therefore protrude from the surface layer. With each copper layer added, the stripes grow in width by one atom, forming internal $\{111\}$ interfaces. The strain relief mechanism gives rise to a characteristic pattern of protruding orthogonal stripes at the film surface. This picture is in marked contrast to the widely accepted continuum theory of epitaxial growth, which predicts a pseudomorphic film growth up to a critical thickness of ~ 8 monolayers.

Because copper grows on Ni(100) in a layer-by-layer-fashion and above 2 ML even in the step flow mode, complications of the diffraction data analysis due to step edges is avoided and Cu/Ni(100) is an ideal system to compare STM and SPA-LEED, two of the most powerful surface analytical tools. The results obtained in this work highlight the pros and cons of both methods.

Contents

1	Introduction	1
2	Experimental	7
2.1	Sample preparation	7
2.2	Setup of the STM-Experiment	8
2.3	Tip preparation and tunneling conditions	15
2.4	SPA-LEED Instrumentation	16
3	Nucleation	19
3.1	Basics of the mean-field nucleation theory	19
3.1.1	General concepts	19
3.1.2	The critical nucleus	23
3.1.3	Lattice symmetry and smallest stable island	25
3.2	Nucleation and submonolayer growth	27
3.2.1	Saturation island density	27
3.2.2	Flux and temperature dependence of the saturation island density	29
3.2.3	Determination of migration barrier and dimer binding energy from the Arrhenius-plot	32
3.2.4	Post-deposition growth and nucleation	38
3.2.5	Post deposition growth observed by SPA-LEED	40
3.3	Conclusions	43
4	Effects of the lattice mismatch on island shapes	45
4.1	STM observation	46
4.2	Ramified islands – an equilibrium state?	50

4.3	Evaluation of ramified island shapes based on the linear chain model	51
4.4	Annihilation of ramified growth shapes by annealing . . .	54
4.5	Conclusion	55
5	Strain relief by internal faceting – STM study	57
5.1	Introduction	57
5.2	Stripe pattern observed by STM	59
5.3	Internal faceting	62
5.4	Strain relief by stacking faults	69
5.5	Interpretation of the AED data by Chambers et al. by internal faceting	70
5.6	Strain relief by a dislocation network	73
5.7	Conclusion	74
6	Strain relief by internal faceting – SPA-LEED study	75
6.1	Introduction	75
6.2	Characterization of stripe pattern	76
6.3	Mosaic formation and characterization of the dislocation network	82
6.4	Limits of strain relief by internal faceting	83
6.5	Conclusion	86
7	Growth kinetics in the multilayer range	89
7.1	Nucleation and surface roughness at multilayer coverage .	89
8	Conclusion	93
	Bibliography	97
	Acknowledgements	105

Chapter 1

Introduction

The tailoring of structures on the nanometer scale is of basic as well as technological interest. There are vastly varying fields of applications, where the realization and understanding of microscopic structures is mandatory, as shall be demonstrated by two examples:

- In the semiconductor industry the development of integrated circuits pushes miniaturisation to its limits. The semiconductor laser is a related example. Without its realization the mass production of compact disc players (their reading device contains such a laser) would not have been possible. The complexity achieved nowadays in such devices can perhaps best be illustrated by an infrared laser constructed recently at AT&T Bell labs: Its construction necessitated more than 500 layers of different semiconductors to be piled up in a perfectly calibrated manner [FCS⁺94].
- In heterogenous catalysis the active sites of a surface are very often defects like dislocations, step edges, kinks etc. [ZWTE96]. Particularly important examples are provided by the platinum-iridium and nickel-copper catalysts used in the hydrogenation and reforming of hydrocarbons. Careful experimental studies have shown that in these systems the active sites for catalysis are represented by small aggregates of one of the two metals. The other metal provides a stable support for these aggregates, and the appropriate conditions (in terms of structure, surface exposition and electronic properties) for their functioning [Sin83].

The examples given above highlight the importance of the nanoscale structure. A crucial point common to the first two examples is the fabrication of smooth, defect free thin films. Defects such as dislocations introduce electronic gap states, and even a small concentration of these gap states may be sufficient to obstruct the success of a heteroepitaxial device. Here, results from basic research can help to decide which types of material are liable to grow almost defect free, and if the use of special techniques – specific growth conditions, surfactants etc. – can improve thin film quality and device performance. However, elucidating when and under which conditions the growth will be perfect is still cumbersome.

The example of the heterogeneous catalysis is insofar an inverse example, as here the ‘tailoring’ of surface structure will demand a maximum number of active sites, i.e. defects. A further source of complication – but also a chance for developing materials with new, interesting properties – is the fact that in thin films metastable structures can be created which are non-existent in the bulk phase. A prominent example is the fcc¹ iron found in thin films on Cu(100) (under normal conditions, iron is bcc²) [BF95, TFW92], which shows interesting magnetic properties [SVK96]. Another example is the catalyst of the Haber Bosch process. There is strong evidence that the site of catalytic activity are iron (111) faces. Normally, (111) faces are unstable, but in the specific case of the Haber-Bosch catalyst this surface is stabilized by the matrix [HHS96].

The prerequisite for the current ‘boom’ in surface science was the advance in the ultra-high-vacuum (UHV) techniques in the past three decades. Nowadays, base pressures of $\sim 10^{-10}$ mbar are routinely reached. These extremely low pressures are in almost all cases indispensable if one wants to prepare clean, well defined surfaces and to retard re-contamination sufficiently long for performing measurements.

A large impetus was the invention of the scanning tunneling microscope (STM) by Binnig and Rohrer [BRGW82, BR82] in 1981, rewarded with the 1984 Nobel price in Physics. In an STM-experiment, a sharp tip is brought into close proximity (sub-nanometer) of the conducting or semiconducting surface. Applying a bias U between tip and sample results in electrons tunneling across the small gap between tip and surface. The tunneling current I drops very quickly – following an ex-

¹fcc: face-centered-cubic

²bcc: body-centered-cubic

ponential law – with increasing sample-tip distance. The sample-tip distance (z -movement) is controlled by a piezo-electric ceramic, similar piezo-ceramics allow scanning movements in the x - and y -direction, i.e. parallel to the surface. As a whole 5 interlinked quantities are defined: The 3 spatial coordinates x , y and z of the tip, the tip-sample bias U and the tunneling current I . In the “constant current” mode U and I are fixed, x and y perform a 2D scan and z is controlled such that I is kept constant. Thus $z(x, y)$ can be interpreted as three-dimensional topographic map of the scanned part of the surface. However, other modes (“constant height mode”, tunneling spectrometry) exist and are employed.

The invention of the scanning tunneling microscope spun off many research activities devoted to growth phenomena and a better insight into the underlying microscopic processes could be gained. Many of these studies were devoted to homoepitaxial systems, where complications due to strain or different surface energies are absent. It was hoped that the aquired knowlege could be simply transferred to heteroepitaxial systems, but the effects of strain showed to be more complicated than originally thought [BK96].

In this thesis, we set out to study dynamical and structural aspects of thin film growth, special interest was payed to the influence of kinetic processes. This is best done by choosing a simple model system void of complications due to multicomponent effects, temperature induced phase transitions etc. The study of such a model system allows to define exactly the role of the different atomic processes and their mutual influence. The most simple system is a homoepitaxial one. But, such a system is less interesting for practical applications. In heteroepitaxial systems, the lattice mismatch is an additional parameter resulting in a great variety of strain relieving defect structures. Copper on Ni(100) is a good candidate for a model system to understand the influence of compressive strain, since

- the (100) surface of nickel is not reconstructed.
- for temperatures below ~ 450 K no intermixing, i.e. no alloy formation occurs and the copper-nickel interface is well defined (see below).
- for the investigated temperature range, reevaporation of copper from the nickel surface can be neglected ($p_{\text{Cu}}(500 \text{ K}) = 5 \times 10^{-30}$).

The lattice mismatch or misfit m is defined as

$$m = \frac{b - a}{a}$$

where a and b are the substrate and the overlayer lattice constant, respectively. In the case of the copper on Ni(100) system, the misfit is +2.6 % (the bulk lattice constant of the two face centered cubic (fcc) substances are: $a_{\text{Cu}} = 3.61 \text{ \AA}$, $a_{\text{Ni}} = 3.52 \text{ \AA}$ [JCP]), i.e., copper grows on Ni(100) under compressive strain. In spite of this not negligible misfit, copper was reported to grow on Ni(100) at room temperature in a well pronounced layer-by-layer fashion [CJ75, CCV+86a]. An important part of the thesis is devoted to the study of multilayers. We wanted to find out how the systems cope with the compressive strain and what are the mechanisms for strain relief.

Another main part has been the study of nucleation processes. Since nucleation is mainly governed by kinetics, the study of the nucleation process and its dependence on parameters such as the deposition flux and the temperature allows to determine accurately quantities such as migration barrier or sizes of the critical nuclei. Such a knowledge is fundamental for understanding epitaxial growth. In Chapter 7 we will demonstrate how in the multilayer range, other phenomena such as strain relief strongly influence the thin film morphology. Nevertheless, it will be seen that the detailed knowledge of the kinetic and energetic parameters determined in chapter 3 is necessary to obtain a comprehensive picture of the multilayer growth.

Important studies have been carried out e.g. on the nucleation of silver on Pt(111). Among others, the mean field nucleation theory was successfully verified (for details, see Chapter 3). Pt(111) is a trigonal surface, while Ni(100) has a square symmetry. We have been interested to know whether nucleation theory can successfully be applied to the copper on Ni(100) system, and if the different surface symmetry has an effect on the nucleation behaviour.

The main tool of investigation is scanning tunneling microscopy. Since it is mandatory for the study of kinetic phenomena to have access to a wide range of temperatures, a variable temperature setup was used. Spot profile analysis of low energy electron diffraction (SPA-LEED) was used as complementary analyzing method. Due to its averaging character, the integrating method SPA-LEED yields information on the sur-

face with high precision, while the local probe technique STM shows only a small part of the surface (in this work, a typical image size is $1000 \text{ \AA} \times 1000 \text{ \AA}$). This, however, can be an advantage, as it allows to exclude the influence of step edges and similar defects by imaging areas far away from these defects.

As a third 'tool' of investigation, abundant rate equation simulations were done. These simulations were compared to experimental results. At the current stage of knowledge, the scope is above all to test these theoretical models and to improve them; another aim is to replace costly MBE-experiments by computer simulations.

The following open questions should be answered by this thesis:

- What are the processes underlying growth kinetics? How can the growth of copper on Ni(100) be described quantitatively?
- How do the macroscopic growth parameters (deposition rate, substrate temperature) determine the thin film morphology?
- Can simulations such as rate-equation analysis improve our understanding of thin film growth?
- What is the influence of substrate symmetry at the different stages of growth?
- What are the strain relief mechanisms in the system?
- How can the misfit be reconciliated with the well-pronounced layer-by-layer growth?

And finally, since we were able to combine in this thesis two powerful surface analytical tools:

- What are the pros and cons of reciprocal-space (SPA-LEED) and real-space (STM) methods in the study of epitaxial growth?

Chapter 2

Experimental

2.1 Sample preparation

The hat-shaped nickel crystal was commercially purchased, the precision of the (100)-cut was guaranteed by the manufacturer to be $0.16\text{--}0.25^\circ$. For sample cleaning, we adopted the following procedure:

1. Argon ion sputtering at elevated sample temperature $T_s \sim 550\text{ K}$.
2. Flash annealing. The sample was heated to $1100\text{--}1200\text{ K}$ for about half a minute. However, at the very beginning of the cleaning process occasional flashes to temperatures as high as 1400 K has been proven to accelerate this process [Lin91].
3. Argon ion sputtering at room temperature.
4. Flash annealing.

In both experiments (STM and SPA-LEED), sputtering was done using argon ions having a kinetic energy of about 2.3 keV and 1.1 keV , respectively. Sputtering currents were chosen to be $4\text{--}7\text{ }\mu\text{A cm}^{-2}$, this necessitated argon pressures of $(1\text{--}4)\times 10^{-6}\text{ mbar}$ (STM) or $1\times 10^{-4}\text{ mbar}$ (SPA-LEED), respectively. One sputtering cycle lasted typically $15\text{--}20\text{ min}$. Supposing a sputter efficiency of unity, this corresponds to the removal of $10\text{--}30$ layers. The last sputtering cycle before copper

deposition was always a non-heated one. This was done to avoid contamination of the surface by impurities diffusing from the bulk, above all carbon [Iba86].

This treatment results in a clean nickel surface – impurities (such as carbon etc.) were below the detection limit of Auger electron spectroscopy. The LEED pattern on the fluorescent screen shows sharp spots and no superstructures are found. Using SPA-LEED, a mean terrace width of ~ 160 Å and a mosaic spread¹ of $0.16 \pm 0.02^\circ$ has been detected (see Fig. 6.4). However, due to considerable step bunching, it was always possible to find large terraces of several thousand Angströms.

Copper (Balzers, 99.99 % pure) was deposited by thermal evaporation at growth rates between 5×10^{-5} and 1×10^{-2} ML/s, corresponding to temperatures of the Knudsen cell between 840 and 1150°C. The growth rates have been calibrated from STM images with monolayer coverage. Here, borderline effects and the resulting inaccuracies are minimal. The measured growth rates R were checked to behave according to $R \propto p(T_K)/(MkT_K)$, where M is the molar weight, k is Boltzmann's constant, T_K is the Knudsen cell's temperature and the vapour pressure $p(T_K)$ varies according to Clausius-Clapeyron's equation.

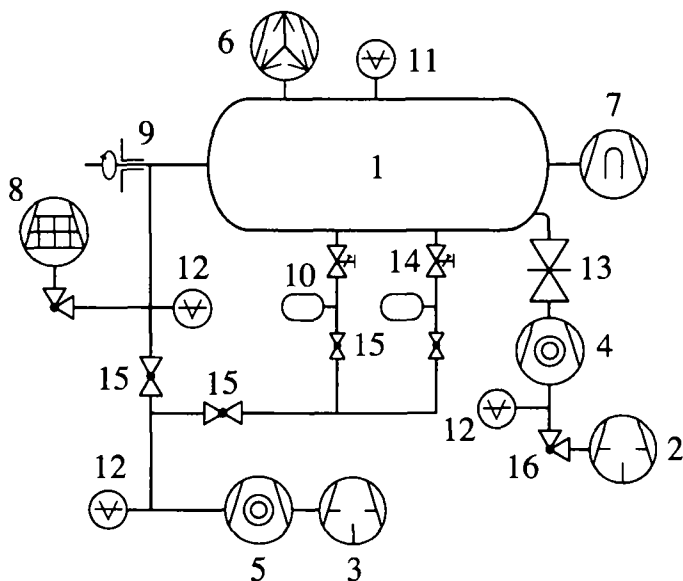
In the SPA-LEED experiment, deposition rates were also monitored by means of a quartz microbalance. The microbalance was calibrated in a series of low temperature experiments. In this temperature range, the intensity oscillations indicating the building-up and completion of a monolayer are well pronounced even at higher coverages (comp. Fig. 7.2).

2.2 Setup of the STM-Experiment

In order to obtain clean, well-defined surfaces all experiments were performed under UHV conditions. The UHV chamber – stainless steel, copper flanged – is pumped by a combination of rotary, turbo molecular, ion and titanium sublimation pumps. A sketch of the setup of the pumping system and chamber is displayed in Figure 2.1. After bakeout ($\sim 150^\circ\text{C}$), a vacuum of better than 2×10^{-10} mbar has been obtained; the total pressure has been measured by ionization gauges.

During STM-measurements, the rotary and turbo molecular pumps

¹for a definition of the mosaic spread, see p.e. [HG94, page 166–167]



- | | |
|--|---|
| 1 UHV chamber | 8 Adsorption pump |
| 2 Two stage rotary vane pump
(16 m ³ /h), Duo 016 B, Balzers,
Lichtenstein. | 9 Differential pumped rotary
feedthrough |
| 3 Rotary vane pump (16 m ³ /h),
Trivac, Leybold, Germany. | 10 Gas inlet system |
| 4 Turbomolecular pump (350 l/s),
340 M, Leybold, Germany. | 11 Ionisation gauge head
(Bayard-Alpert), IE 414,
Leybold, Germany. |
| 5 Turbomolecular pump (15 l/s),
TPD 020, Balzers, Lichtenstein. | 12 Pirani gauge head |
| 6 Ion pump (200 l/s), PID 200N,
Meca2000, France. | 13 Bellows-sealed gate valve |
| 7 Titanium sublimation pump | 14 Leak valve |
| | 15 Seal valve |
| | 16 Seal valve |

Fig. 2.1. Sketch of the vacuum system

are stopped, as the vibrations and sound would render STM measurements impossible, and pumping was done with the ion pump and the adsorption pump ((6) and (8) in Fig. 2.1 only.)

In addition to the STM (homebuilt), the chamber is equipped with the following tools for sample preparation and surface analysis:

- Ion gun for sputtering (Ion gun: homebuilt; power supply: PS-IQE 10/35, Specs, Germany)
- A Knudsen type evaporator for copper deposition (WKC3, W.A. Technology Ltd., England)
- A backview LEED system (SPECTALEED, Omicron, Germany)
- An Auger electron spectrometer: Cylindrical sector analyzer (CSA 300) combined with an electron gun (EKF 50) (Focus/Omicron, Germany)
- Quadrupole mass spectrometer (TRANSPECTOR H200M, Inficon/Leybold, Germany)

The STM employed is a Besocke type [Bes87] (see Fig. 2.2). Basically, the Besocke or 'beetle' STM has the form of a tripod – three piezoceramics tubes forming the legs of the tripod are fixed to an aluminum head – which supports a central piezo tube. Scanning is performed by the inner piezo tube. Due to a specific arrangement of the electrodes the so called single tube scanner [BS86] is able to accomplish all three movements needed for STM image acquisition – z-scan, i.e. control of the tip-sample distance, scanning in x-direction, scanning in y-direction.

The outer piezo tubes, which form the legs of the tripod, serve as piezodrives as well for the coarse tip approach as well for macroscopic steps: Applying an electrical signal of the sawtooth type will result in a stick-and-slip movement of the tripod. Depending on the mode used, the beetle STM will either screw the circular ramp up and down (i.e. it will perform a tip approach), or move sideways across the sample [FWBT89].

Some of the advantages of the Besocke type STM are:

- The design of the "beetle" STM is compact. Due to its "pocket size" and its rigid construction, it is rather robust to external vibrations.

- For operation, the STM is simply placed on the sample. No complicated and possibly fragile sample transfer mechanisms are necessary. As the sample remains mounted to the manipulator during all operations, the realization of a temperature control system for STM *in situ* studies is greatly facilitated. Moreover, this setup is especially adopted for combining STM with other surface analytical techniques.
- There is an internal drift compensation inherent to the Besocke design. As the microscope stands on piezo legs which have the same thermal expansion rate as the central tube scanner holding the tip, to a first order, the tip-sample distance remains unchanged upon temperature variation. This is especially important in variable temperature measurements.

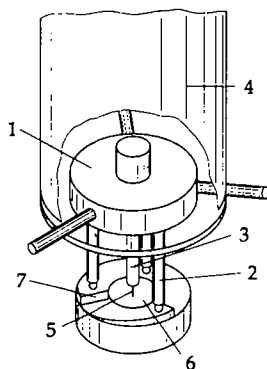


Fig. 2.2. Principle of the “beetle-type”-STM. The body of the STM – consisting of an aluminum hat (1) and 3 piezo legs (2) – is placed onto a circular ramp (7). For the coarse approach between the tip (5) and the sample (6) the STM-“beetle” – driven by a electrical signal provoking a “stick-and-slip” movement – walks down the circular ramp (7). Once the STM is in tunneling range scanning is effected through the inner piezo (3), which is a single tube scanner. The STM beetle is lifted from the sample with the help off a support tube (4).

The sample manipulator is based on a design originally developed by H. Röder in our laboratory [Röder94, BRBK95]. However, several changes were made in the course of the thesis. In order to obtain EELS compatibility, magnetic materials are avoided and all electrical contacts to the sample are shielded. To improve STM imaging performance, a supplementary vibrational damping stage was introduced.

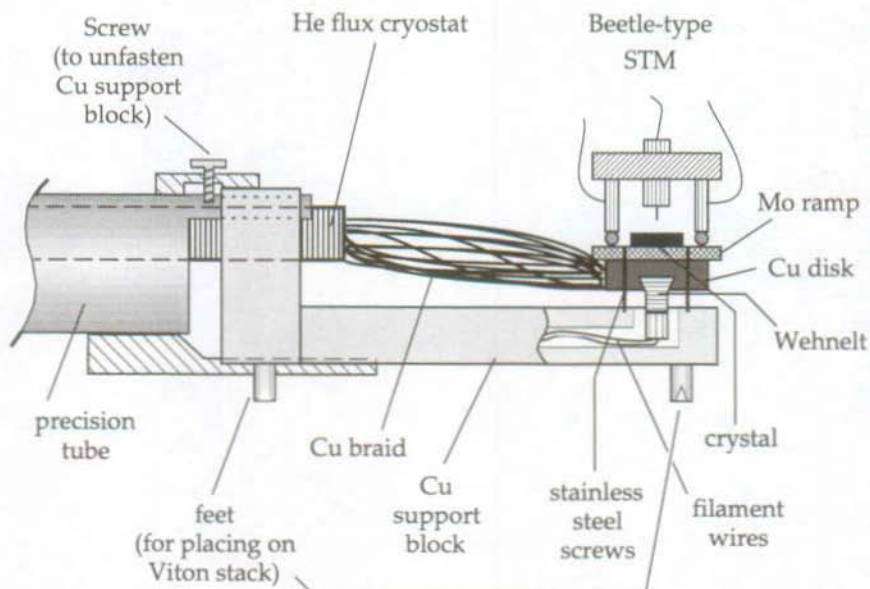


Fig. 2.3. Side view of the sample holder. In STM mode, the copper support block is uncoupled from the precision tube and rests upon a copper-plate stack (not shown).

Fig 2.3 shows a sketch of the sample manipulator. One can distinguish three functional units: The actual sample holder comprising the circular ramp for tip approach and as well the *in situ* part of temperature control system, the copper support block, and the precision tube connected to a long travel manipulator including the cryostat.

The sample crystal is hat-shaped, the actual sample surface corresponds to approximately half a square centimeter. At his brim, the crystal is clamped to a copper support by means of a molybdenum ring; the later provides the circular ramp for tip approach. The sample is electrically isolated from both, molybdenum ring and copper disk by sapphire plates. Heating is done either by radiation or by electron bombardment from a filament (Tungsten/Rhenium, $\phi=0.2$ mm) mounted at the backside of the sample. For cooling, this unit is connected to a cryostat via a soft copper braid. Temperature is measured by an chromel-alumel thermocouple spot-welded to the sample. The sample unit is rigidly attached to the copper support block, care was taken to minimize thermal connections in order to assure small thermal equilibration times [DKZC86].

During all operations except STM measurements, the copper support block is attached to the precision tube of a commercial long travel translational manipulator (Omniac 600, Vacuum Generator, England) combined with a rotary feedthrough. The cryostat, which is cooled either with liquid Helium or cold Nitrogen gas, is placed at the interior of the precision tube. For STM measurements, the copper block with the sample unit can be detached from the precision tube and is placed upon a stack of copperplates damped by Viton pieces to eliminate high frequency mechanical noise. In order to suppress low-frequency noise (building vibrations), the experiment is equipped with a second damping stage: The UHV chamber as a whole can be lifted from its usual supports and hung to steel springs. Thus, the main sources for mechanical noise during STM measurements are effectively eliminated. Outside noise is damped by the combined steel spring/viton stack damping system, the transmission of vibrations from the cryostat caused by the flow of the cooling agent to the sample is hindered by the soft copper braid. Sample and microscope are vibrationally decoupled from the environment.

Tests indicate 800 K to be the maximum sample temperature possible for STM measurements. Beyond this limit the piezolegs of the beetle STM are excessively heated and there is a strong risk for the piezo material (Vibrit 420, Siemens, Germany) to depolarize irreversible, causing the destruction of the STM 'beetle'. The lowest temperature we accessed with the STM was 90 K. However, optimization of the cooling system was never done, but the design has proven to be apt for STM measure-

ments at temperatures as low as 30 K [Röder94]. In this work we did not exhaust the full dynamic temperature range and only results obtained between 100–450 K will be presented.

STM measurements at temperatures below room temperature were performed with continuous flow of cooling agent, the precise temperature was maintained by heating from the backside with the filament. The measurement of sample temperature and its control was done by a PID (= proportional-integral-differential) controller (Eurotherm, Eurotherm Ltd., England). The relative temperature stability corresponds to 0.1 K, temperature measurements had been tested by immersing the sample into liquid nitrogen and a acetone/solid carbondioxid cold bath. The accuracy of temperature measurements was estimated to be 2.5 K above and 5 K below 200 K.

The scanning ranges were calibrated by imaging the Chevron reconstruction on the Au(111) surface [BBEB90]. Some of the characteristics of our ‘Beetle’-STM are assembled in Table 2.2. Two STM electron-

Sensitivity x, y-scan:	$(120 \pm 5) \text{ \AA/V}$
Sensitivity z-scan:	$(12.0 \pm 1.5) \text{ \AA/V}$
Scanning range (Besocke) ^a :	$4800 \text{ \AA} \times 4800 \text{ \AA}$
Scanning range (RHK) ^a :	$20000 \text{ \AA} \times 20000 \text{ \AA}^b$.

^arefers to the control-electronics used.

^bValue deduced by extrapolation. In our own testings, we did not exceed $10000 \text{ \AA} \times 10000 \text{ \AA}$

Table 2.1. Characteristics of the used ‘Beetle’-STM

ics were used: First, a relatively simple, home-built control electronics was employed, which corresponds to the Besocke “beetle” STM electronics [Bes]. Later, a high performance electronics (STM 2000, RHK, USA) was adopted to our system. The signal to noise ratio of the RHK electronics is much better, it is equipped with a 16-bit A/D converter (before: 8-bit converter) resulting in a markedly finer graduation of the gained topographic height information. Various additional features such as electronic real-time plane compensation, tunneling spectroscopy, improved image treatment and data evaluation are implemented. The evo-

lution of microscope performance can best be illustrated on the example of the aluminum on Au(111) system [FBF⁺]. With the original setup, we were able to image the Chevron reconstruction of the Au(111) surface, the quality of these images was improved by the introduction of the viton stack. However, it was not possible to image the gold reconstruction and small aluminium islands simultaneously. This task was accomplished using the RHK electronics with the higher resolution.

2.3 Tip preparation and tunneling conditions

The STM tips were prepared by electrochemical etching of a polycrystalline tungsten wire ($\phi = 0.25$ mm) in 2 n sodium hydroxide solution as described in [Röd91, MBT88]. A tip prepared in such a way would not give a satisfactory results without further treatment. Once the tip had been mounted in UHV, one or several of the following *in situ* tip preparation recipes had to be applied.

- Changes of the applied voltage during tunneling - either in the form of a sharp pulse [WWB⁺89] or by increasing the voltage for a limited time and then decreasing it slowly [Röd91] - may lead to exchanges of material between the tip and the nickel sample.
- Controlled tip “crashes”, i.e., the tip is indented into the sample by several nanometers [BSS⁺95]. By doing so, the tip may pick up a cluster of sample atoms and tunneling will be effected by the resulting nanotip.
- Sputtering of the tip: Here, a high negative voltage is applied to the tip (~ 250 V) and the tip is approached to the sample, until a weak field emission current can be measured (~ 10 μ A). Argon gas is let into the chamber, the measured current between tip and sample has to raise markedly (by a factor of 5, approximately). This raise is caused the noble gas ions which are ionized by the strong electrical field in the gap between tip and sample and sputter the later. The progress of the sputtering process can be monitored by a slow descent of the sputtering current. On a first try, often

the tip behaves in an unstable way, i.e., suddenly the sputtering current drops to zero. The loss of tip material causing the drop can be equivalent to a shortening of the tip of 100 Angströms or even more. In such a case, the procedure described above has to be repeated again. Ideally, one observes a slow and steady decrease of the measured current over a time span of 5–15 min. This procedure removes dirt such as organic materials or oxides from the tip.

In any case, there is no foolproof way for tip preparation. After all, tip treatment is a try-and-error process, during which one of the procedures (or a combination of several) has to be repeated until satisfactory conditions are obtained.

Once a satisfactory tip shape had been obtained, we moved away from tip preparation area since it had usually been spoiled in the process. Typical tunneling conditions are bias voltages of 0.2–2.0 V and currents of 0.5–15 nA. We never observed noteworthy changes in the imaged topography due to variations of tunneling current or voltage. The scanning frequency was about 10 Hz in the fast x-direction. Since our main interest is the topography of the studied surfaces, STM images were invariantly recorded in the constant current mode.

While we were using the “Besocke”-electronics, many of the images were recorded in the differential mode (for an example, see Fig. 3.2 (a)–(c) or Fig. 5.10). In this mode the original input signal – the height information z – is electronically differentiated and a high pass filter with a cut off frequency of 33 Hz is applied to it. The resulting signal – to a first order proportional to $\partial z/\partial x$ – is recorded. Images which were recorded in differential mode show the surface topography as illuminated from the left.

2.4 SPA-LEED Instrumentation

The SPA-LEED measurements have been performed in an UHV chamber at the Institute of Solid State Physics (Hannover University) (base pressure: 5×10^{-11} mbar); the experimental setup is described in detail in Ref. [Sch95].

For the experiments we have used the ion sputter gun for sample preparation, the auger spectrometer to check the impurity level and the

quadrupole mass spectrometer for residual gas analysis. Figure 2.4 shows a scheme of the apparatus in the plane of the SPA-LEED instrument.

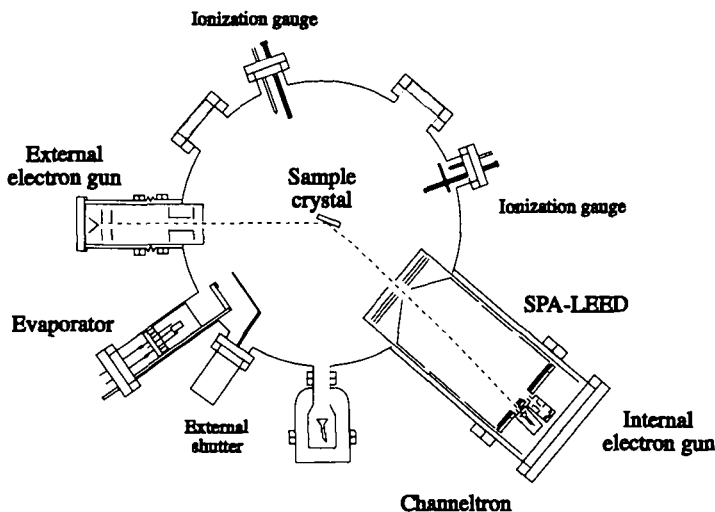


Fig. 2.4. Section of the analyzer stage of the SPA-LEED UHV-chamber

The resolution of the SPA-LEED [SMH86], is characterized by a transfer width of 2000 \AA [Wol], that means defect structure with a characteristic length of $\sim 0.2 \mu\text{m}$ can be detected [EK85].

In addition to internal electron gun of the SPA-LEED, an external gun is mounted on the chamber. Therefore, it has been possible to monitor the surface morphology during growth. The angle of incidence is 112° for the external and 8° for the internal electron gun.

The sample manipulator resembles insofar the STM-manipulator, as the sample potential is free floating, heating is done by a tungsten wire mounted at the backside of the sample, and the temperature is measured by a thermocouple (chromel-alumel) and adjusted by a PID-controller. Therefore, the conditions for experiments are comparable in the STM chamber at EPF Lausanne and in the SPA-LEED chamber at Hannover University.

Chapter 3

Nucleation

3.1 Basics of the mean-field nucleation theory

3.1.1 General concepts

Growth by MBE is a non equilibrium process. Nevertheless, thermodynamic arguments can be applied in MBE scenarios. One well-known example is the use of Bauer's criterion [Bau58], where the occurrence of different growth modes (Frank-van der Merwe (= layer-by-layer), Volmer-Weber (= islands), and Stranski-Krastanov growth (= layer + islands)) is explained by comparing the corresponding interface free energies.

Bauer's criterion works reasonable well in the high temperature range, but, especially at low temperatures, the non-equilibrium character of growth dominates and a description based upon a kinetic treatment is more appropriate. The mean-field nucleation theory (for reviews, see [VSH84, Rei86, Zan93]), is based on such an approach: Rate equations accounting for the underlying atomic processes are derived and the resulting differential equations are solved. One result of this theory proved by experiment is a scaling between the density of stable islands n_x , the deposition flux R and the surface diffusion constant \mathcal{D} :

$$n_x \propto (\mathcal{D}/R)^{-\lambda} \quad (3.1)$$

R is one of the external parameters; variations of the diffusion constant \mathcal{D} can be realized by changing the substrate temperature T_s : $\mathcal{D} = 1/4 \nu_0 \exp(-E_m/(kT_s))$. E_m denotes the activation energy for monomer terrace migration, k is the Boltzmann constant and the preexponential factor ν_0 is the attempt frequency. The number four in the denominator accounts for the fact that, on a square lattice, there are 4 equivalent diffusion routes out of an adsorption site. In the expression (3.1), the scaling exponent χ depends on the desorption rate, the dimensionality of the deposit and the size of the critical nucleus. In the case of copper on Ni(100) the film grows mainly in a layer-by-layer fashion (see chap. 5), hence the dimensionality of the deposit is 2. Desorption can be neglected in the temperature range up to 400 K, since at this temperature the nominal vapour pressure corresponds to $\sim 10^{-35}$ mbar [Lid95]. Accordingly, we restrict the discussion of the rate equation analysis and the mean-field nucleation theory to the case of 2D growth and complete condensation.

If one assumes, in addition, the dimer to be the smallest stable island, the growth is governed by the following atomic processes:

- (i) Deposition of an atom on the surface.
- (ii) Adatom diffusion, until
 - a) it collides with another adatom forming an immobile dimer.
 - b) it hits an existing cluster and is incorporated.
- (iii) Coalescence of islands.
- (iv) Direct impingement, i.e., adatoms are deposited on top of clusters or monomers, or at neighbouring sites.

and the rate equations for the monomer density n_1 and the density for the clusters n_x can be written as:

$$\frac{dn_1}{dt} = R - 2\mathcal{D}\sigma_1 n_1^2 - \mathcal{D}\sigma_x n_1 n_x - R(Rt - n_1) - 10Rn_1 \quad (3.2)$$

$$\frac{dn_x}{dt} = \mathcal{D}\sigma_1 n_1^2 + 5Rn_1 - U_c \quad (3.3)$$

n_1 and n_x are given in units of (adsorption site) $^{-1}$. The monomer density increases by the deposition rate R . It is reduced by the dimer formation

(second term in 3.2), by migration to a stable island¹ (third term), and due to direct impingement upon clusters (fourth term) and monomers (fifth term). The latter term is correct in the case of a square lattice. The factor ten accounts for the fact that a dimer is created either when the monomer directly arrives on-top of the adsorbed monomer, or on one of its four neighboring sites; these five channels have to be doubled since two monomers disappear by the creation of a dimer. In the fourth term (the cluster impingement term) the deposition of monomers onto neighboring sites of a stable islands is neglected for simplicity.

The density of the stable islands, on the other hand, increases with the creation of dimers due to monomer migration (first term of (3.3)) and due to nucleation events caused by the deposition of an atom on top of a monomer or its nearest neighbor sites (second term). The coalescence reduces the density of stable islands (third term). U_c describes the diminution of island density due to coalescence. There is still no general analytical expression for the coalescence term. However, according to [VSH84, eqn. 2.11] one can set

$$U_c = 2n_x \frac{dZ}{dT} = 2n_x \left(-\frac{dn_1}{dt} + R \right), \quad (3.4)$$

which yields satisfactory results for small island sizes. Z denotes the fraction of the surface covered by stable cluster.

The capture numbers σ_1 and σ_x can be considered as an effective cross section for adatom capture. Note one fundamental simplification: Instead of solving a set of differential equations, one equation for each cluster size x , all clusters of size $x \geq 2$ are lumped together and are considered to belong to the same specimen whose overall behaviour can be described in one expression only (3.3). This approach gives exact quantitative results, if one succeeds to determine ‘good’ capture numbers σ . In the last decades several concepts for the evaluation of capture numbers have evolved:

In the **geometrical concept** [Zin71], the capture number is identical to the island diameter as it is seen by the approaching monomer:

¹Though the term “cluster”, “nucleus” and “island” can be used interchangeably, I will use the term “cluster” to denote any small group of atoms and “nucleus” to denote a cluster whose size corresponds more or less to the smallest stable cluster. “Island” refers to large clusters and represents the objects that can be detected after the growth experiment.

$\sigma_x = 2 + (\text{islandsize})^{1/\mathcal{H}}$. Effects of the island shapes are included in the exponent $1/\mathcal{H}$. In the case of fractal islands, one sets $\mathcal{H} = 1.7$. The constant 2 accounts for the fact that the effective island diameter for adatom capture has to be augmented by the sites adjacent to the island perimeter. The geometric concept is only exact in the case of small islands, as it ignores that any nucleation site (island, step edge) is surrounded by an area of reduced adatom concentration (denuded zone).

The **uniform depletion approximation** addresses the problem by placing one island in a ‘sea’ of monomers. Then, the spatial convolution of adatom concentrations is calculated according to Fick’s law, and the capture numbers are deduced. Further improvement can be obtained by taking into account the interaction of nucleation sites. In the **lattice approximation**, islands are placed upon a square lattice, the diffusion problem is treated in a similar way as in the uniform depletion approximation. An analytical expression for σ_x that depends only on coverage is obtained [Ven73, eqn. 22]. Rate equation analysis based upon the lattice approximation reproduces the evolution of experimental island densities nicely [BRBK94a, BHM+96]. A still higher precision can be obtained by the approach proposed by **Bales and Chrzan** [BC94], where the artificial regular placement of islands on a square lattice has been abolished. Their self-consistent solution takes into account the statistic nature of island distances. However, even this sophisticated approach fails to reproduce correct island size distributions, as it does not properly include island-island correlations.

Using any of the approximations stated above, evaluation of (3.2) and (3.3) leads to qualitatively correct results. One obtains the three growth regimes: In the beginning the transient or nucleation regime small cluster are formed by nucleation, an increase in coverage will increase the number of islands while the size of the nuclei remains unchanged. Later on, capture of single adatoms by already existing islands is becoming predominant, until – in the saturation regime – island density remains constant. At still higher coverage, the coalescence of islands sets in. Also, a quantitative evaluation of this simple growth scenario yields a scaling behaviour in agreement with relation (3.1). In this evaluation χ is found to be $1/3$.

3.1.2 The critical nucleus

In the growth scenario depicted above, the dimer formation was assumed to be irreversible. In other words: The dimer was the smallest stable island, or, the size of the “critical nucleus” is $i = 1$. “Critical nucleus” means that one atom more will yield a stable cluster. But what happens when the bond energy is not sufficient to retard thermal dissociation of the newly formed dimer during deposition? An exact way to address the problem is to add rate equations and thereby to keep track of each class of subcritical and critical clusters. In the case of $i = 3$, and the assumptions mentioned above, one obtains four coupled rate equations:

$$\begin{aligned} \frac{dn_1}{dt} = & R + 2\nu_2 n_2 + \nu_3 n_3 - 2\sigma_1 \mathcal{D}n_1^2 - \sigma_x \mathcal{D}n_1 n_x - \sigma_2 \mathcal{D}n_1 n_2 \\ & - \sigma_3 \mathcal{D}n_1 n_3 - 10Rn_1 - R(Rt - n_1) \end{aligned} \quad (3.5)$$

$$\frac{dn_2}{dt} = \sigma_1 \mathcal{D}n_1^2 - \nu_2 n_2 + \nu_3 n_3 - \sigma_2 \mathcal{D}n_1 n_2 + 5Rn_1 - Rn_2 \quad (3.6)$$

$$\frac{dn_3}{dt} = \sigma_2 \mathcal{D}n_1 n_2 - \nu_3 n_3 - \sigma_3 \mathcal{D}n_1 n_3 + Rn_2 - Rn_3 \quad (3.7)$$

$$\frac{dn_x}{dt} = \sigma_3 \mathcal{D}n_1 n_3 + Rn_3 \quad (3.8)$$

(In the above equations, coalescence is neglected.) ν_2, ν_3 are the rate constants for dimer respectively trimer dissociation. One avoids a detailed analysis and the further deduction is based upon the assumption that for clusters $\leq i$ equilibrium conditions prevail. In this case, one can use a result of statistic thermodynamics and write according to Walton [Wal62]:

$$n_i \propto n_1^i \exp\left(\frac{E_i}{kT}\right) \quad (3.9)$$

E_i is the total binding energy of a i -sized cluster. Now, the set of $(i + 1)$ rate equations can be reduced to only two, as the densities of subcritical clusters n_1, n_2, \dots, n_i can be deduced from the monomer density. One of the consequences of the concept of the critical nucleus is a scaling exponent χ , whose value depends on the size of the critical nucleus. In the case of 2D-growth and complete condensation, χ writes

$$\chi = \frac{i}{i + 2} \quad (3.10)$$

and, as a final result, one can obtain an expression for the island density of stable islands:

$$n_x \cong \eta(\theta) \left(\frac{D}{R} \right)^{-\lambda} \exp \left(\frac{E_i}{(i+2)kT} \right) \quad (3.11)$$

Here, $\eta(\theta)$ is a function of coverage θ . Numerical values for $\eta(\theta)$ can be found in [VSH84, Fig. 6(c)]. In the saturation regime, $\eta(\theta)$ is almost constant. Hence, in this regime, minor fluctuations in coverage will have no effect on island densities and one can safely assume the temperature T and the flux R to be the only relevant external parameter.

The mean field nucleation theory has been used to extract microscopic values such as the activation energy of terrace adatom diffusion E_m or the size of the critical nucleus [BMC92, RBBK93, SPD93, BRBK94a, BHF⁺94, GKB⁺94, BHM⁺96, LMJ⁺96]. In this context, stability refers to the time scale of the deposition experiment (which may last only a fraction of a second), and it can not be taken for granted that a “stable” cluster will be stable on the time scale of the following measurement (which may take several hours). In the saturation regime islands are usually much larger than the critical nucleus and the surface can be imaged reproducibly over hours under isothermal conditions without any change.

In a series of experiments performed at 300–350 K, we tested this time invariance. STM imaging did not reveal any changes in the submonolayer films, neither in island position nor in island size or shape. Also, quenching the sample immediately after closing the shutter and performing the STM measurements at low temperatures (~ 140 K) gave identical results as compared to STM data obtained at deposition temperature.

The mean field nucleation theory had been tested by Brune *et al.* in the following way: The authors determined the critical island size – independent from nucleation theory – for the heteroepitaxial system Ag/Pt(111), by direct measurement of the mean island sizes in the very initial stages of nucleation [BRBK94a], and by measuring the temperature threshold for Ostwald ripening of dimers [RHB⁺93]. Therefore the rate dependence as well as the Arrhenius behaviour of the saturation island density at a known critical cluster size of $i = 1$ allowed a direct test of nucleation theory [BRBK94a], which has been proven for a surface system with a trigonal lattice. This theory should be applicable for Cu/Ni(100), too.

3.1.3 Lattice symmetry and smallest stable island

The concepts mentioned above are continuum models which do not account for the symmetry of the particular system. In the following, we will discuss the impact of the substrate symmetry on the nucleation behaviour. The consequences for critical nuclei sizes will be elucidated.

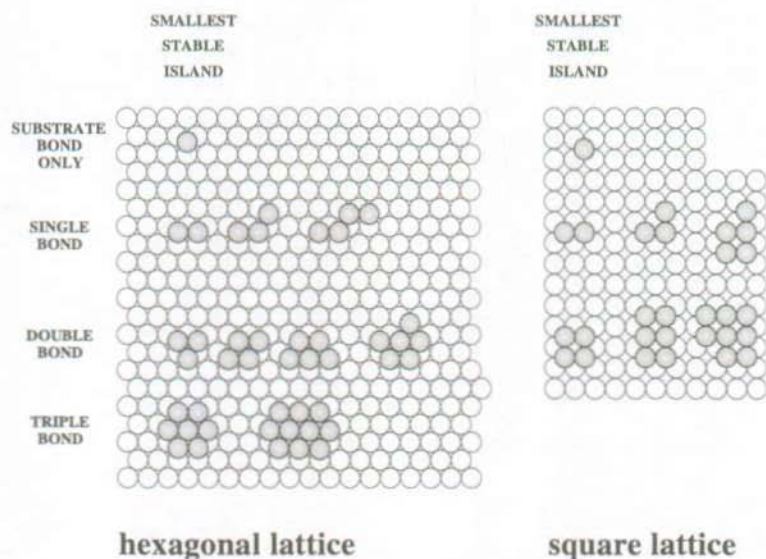


Fig. 3.1. Impact of substrate symmetry on the cluster stability. Clusters of various sizes and forms are listed according to their stability, i.e. whether the detachment of an atom involves the breaking of a single, double or triple bond. In the case of statistic growth (no adatom diffusion), the monomer is considered to be the smallest stable island (i.e. $i = 0$). If single bonding is sufficient to retard thermal dissociation, the dimer is the smallest stable island ($i = 1$), regardless of substrate symmetry. However, if clusters are only stable if dissociation involves the breaking of a double bond, the substrate symmetry does become important: On a hexagonal substrate, this will result in the smallest stable island being a trimer ($i = 2$), while on a square lattice, the smallest stable island will be a tetramer ($i = 3$). Concerning the consequences for the nucleation behaviour, see text.

For very low temperatures one may find that the monomers do not migrate at all (statistic growth with monomers being immobile, i.e., $i = 0$). With increasing temperature, the monomers start to migrate and to form dimers which are stable ($i = 1$). Increasing the temperature further, dimers dissociate, and either the trimer becomes the smallest stable island ($i = 2$), or the smallest stable island corresponds to a tetramer ($i = 3$) and so on. The classic continuum model ignores the adsorption site geometry of the substrate which does not matter for the critical island sizes $i = 0$ and $i = 1$. For greater island sizes, however, the binding energy substantially depends on the geometric arrangement of the atoms and the choice of possible cluster configuration is dictated by the lattice symmetry. While on a trigonal or hexagonal surface dimer dissociation involves breaking of a single bond, trimer dissociation of two bonds, and heptamer dissociation the breaking of three bonds (see Fig. 3.1, left hand side), on a square lattice the dissociation of both dimer *and* trimer is characterized by single bond breaking and therefore associated with similar dissociation barriers (see right side of Fig. 3.1). Hence, on square lattices, one expects a direct change from $i = 1$ to $i = 3$ due to the transition from single to double bond breaking. The atoms of compact islands which contain 4 atoms have two neighbours in the ad-layer. Above $i = 3$, there is no well-defined behaviour since all islands on square lattices are characterized by single or double bond breaking. Thus, islands which mark a notable rise in binding energy and hence should play a distinct role in the nucleation scenario are expected to be the dimer and the tetramer for square symmetry. On hexagonal surfaces, these islands might be the dimer, the trimer and the heptamer.

The arguments above imply that, to a first order, far and medium range interactions can be ignored and next neighbour binding is the only relevant contribution to the heat of formation of small clusters. Applying this argument to a square lattice, one can determine the binding energies E_2, E_3, E_4, \dots of the variously sized clusters by a simple bond counting argument – if one knows the energy E_b of a single bond.

$$E_2 = E_b, \quad E_3 = 2 * E_b, \quad E_4 = 4 * E_b, \dots \quad (3.12)$$

3.2 Nucleation and submonolayer growth

3.2.1 Saturation island density

The first step of the analysis according to nucleation theory is the experimental verification of the saturation island density. Figure 3.2 shows the evaluation of island density and shapes as seen by STM. Image (a) ($\theta = 0.04$ ML) shows the situation in the nucleation regime, and an increase in coverage will increase the island density, as can be nicely seen by comparing image (a) and (b). Image (b) ($\theta = 0.09$ ML) as well as image (c) ($\theta = 0.15$ ML) are both situated in the saturation regime. The island density in both images is almost constant. Note, the larger islands in image (b) and (c) are not compact. Occurrence of ramified islands is not restricted to substrate temperatures of 345 K (comp. Fig. 3.4); the physical reason for the formation of irregular shaped islands will be discussed in the next chapter.

Coalescence becomes more important at higher coverage (image (d), $\theta = 0.35$ ML) resulting in a marked drop in island density (image (e), $\theta = 0.65$ ML). Image (f) finally shows the situation at nearly monolayer coverage, no single islands can be found.

Quantitative evaluation of the island density as a function of coverage is shown in Figure 3.3 for a substrate temperature of 345 K and two different deposition rates. In the quantitative evaluation of the STM data (e.g.: determination of island density) the thermal drift has been determined by comparing characteristic features at successively obtained images and the island density has been corrected accordingly. The influence of structural defects such as steps has been excluded by depicting areas far away from steps.

In the coverage range between 0.1 and 0.2 ML (which is the expected coverage for the saturation regime) the island density remains constant. For the low flux measurement ($R = 1.5 \times 10^{-3}$), the island density is nearly constant over a wide coverage range (0.01-0.50 ML). Therefore, at 345 K, the choice of the coverage to obtain the saturation island density is not crucial. A coverage between 0.08 and 0.12 ML is used for the present study.

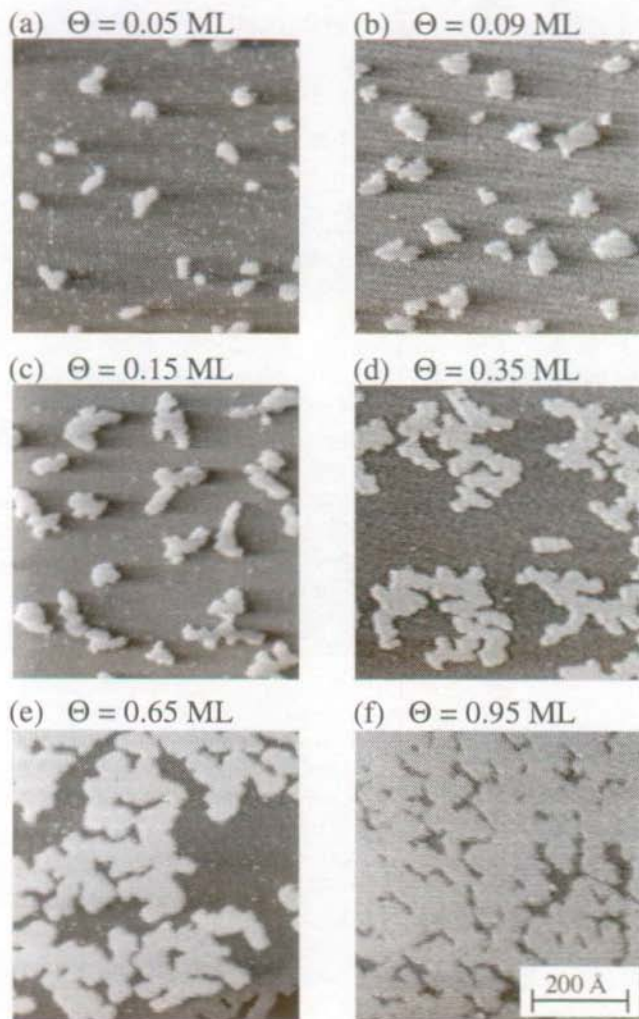


Fig. 3.2. STM images characterizing the evolution of thin film morphology and island density for submonolayer growth of copper on Ni(100) with coverage. Temperatures (345 K) and deposition rate (6×10^{-3} ML/s) remained constant. Images (a)–(c) were recorded in the differential mode, images (d)–(f) in the absolute height mode.

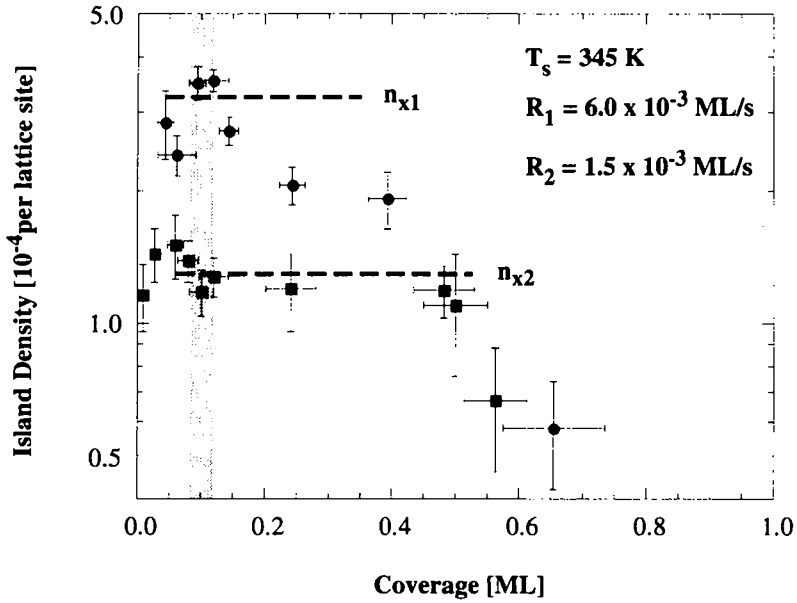


Fig. 3.3. Island densities versus coverage for two different fluxes (1.5×10^{-3} ML/s and 6.0×10^{-3} ML/s) at a substrate temperature of 345 K.

3.2.2 Flux and temperature dependence of the saturation island density

The variation of the saturation island density with substrate temperature is characterized in Figure 3.4, showing four STM images obtained at fixed deposition rate and coverage. The decrease in island density over orders of magnitude with substrate temperature is clearly visible. These island densities directly reflect the adatom mobility, which depends exponentially on substrate temperature.

Figure 3.5 shows the measured temperature dependence of the saturation island density as Arrhenius plot at a coverage of about 0.1 ML

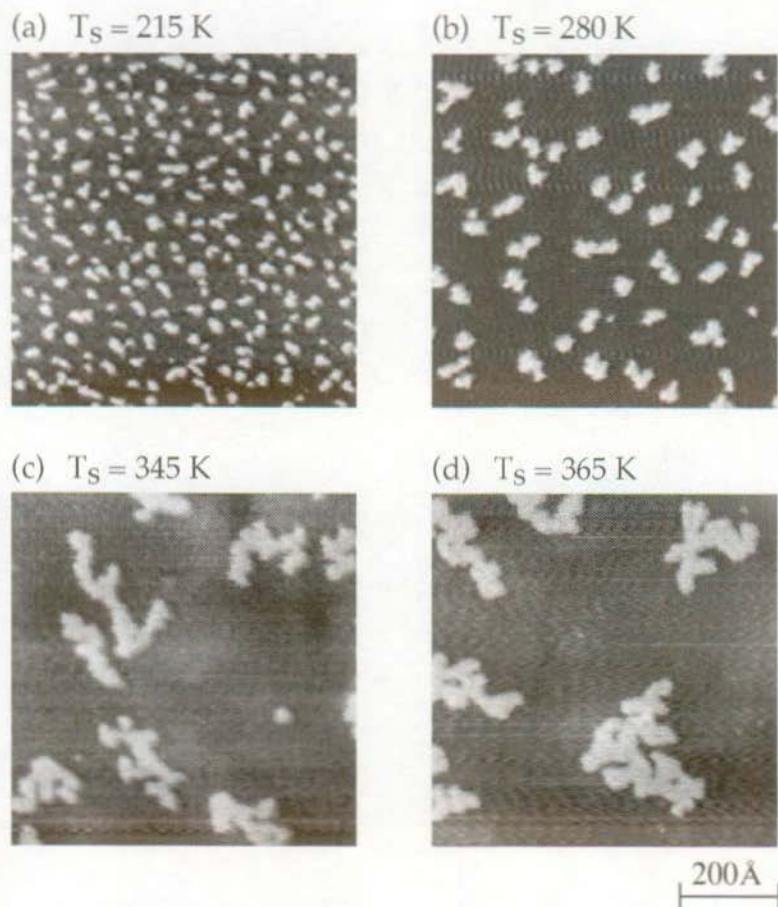


Fig. 3.4. STM images characterizing the saturation island densities for the submonolayer growth of copper on Ni(100) at different growth temperatures and fixed deposition rate (1.5×10^{-3} ML/s) and coverage (0.1 ML).

and a flux of 1.5×10^{-3} ML/s. One can clearly distinguish between three different nucleation regimes which are labeled post-nucleation, $i = 1$, and $i = 3$, respectively. Below 160 K, the island density does not vary with temperature indicating statistic growth with $i = 0$. However, the mean island size of 4.5 atoms is too large. For statistic growth on a square lattice at 0.1 ML, a mean island size of 1.25 atoms is obtained from percolation theory [SG76]. Therefore, statistic growth can definitely be excluded. The physical reason for the plateau in the Arrhenius plot is the island formation and the incorporation of monomers into existing islands after deposition (see Sect. 3.2.4).

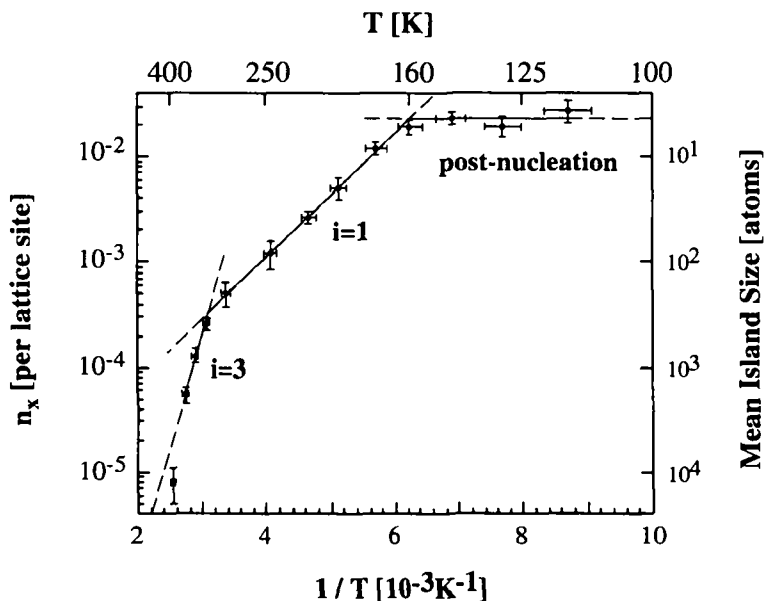


Fig. 3.5. Arrhenius plot of the measured saturation island density of copper on Ni(100) (flux: 1.5×10^{-3} ML/s; coverage (0.10 ± 0.02) ML).

The two regimes entered above 160 K and 320 K, respectively, have been labeled corresponding to the sizes of the critical nuclei. In order to establish these sizes, we have measured the rate dependence of the island density $n_x(R)$ at three different substrate temperatures – 145, 215, and 345 K – each located in the center of the labeled regions in the Arrhenius plot. Using relation (3.1) and (3.10), it is straightforward to determine the size of the critical nucleus. For the different critical nuclei, the exponent χ corresponds to $1/3$ for $i = 1^2$, $1/2$ for $i = 2$ and raises to $3/5$ for $i = 3$. The double-logarithmic plots of the island density versus flux in Figure 3.6 show that the exponent χ corresponds to (0.32 ± 0.01) at 215 K and to (0.58 ± 0.02) at 345 K which clearly proves that the monomer is the critical nucleus at 215 K ($i = 1$) and the tetramer becomes the smallest stable island at 345 K ($i = 3$). In addition to the rate dependency of the saturation island density, one can use the scaled island size distribution and scaling theory to extract the size of the critical nucleus. These size distributions are presented in Figure 3.7 for three substrate temperatures. They show exactly the expected behaviour, $i = 0$ for 160 K, $i = 1$ for 215 K, and a distribution closely resembling that of $i = 3$ for 345 K, each at a deposition rate of 1.5×10^{-3} ML/s. The coverage corresponds to 0.1 ML for 160 and 215 K. For 345 K, however, the coverage chosen is much smaller. At such a temperature, higher coverage leads to comparatively large islands which become irregular shaped. This leads to a significant broadening of the size distribution.

3.2.3 Determination of migration barrier and dimer binding energy from the Arrhenius-plot

Because the sizes of the critical nuclei are known, the migration barrier of a single adatom E_m , the dimer bond energy E_b as well as the attempt frequency ν_0 can be determined analyzing the Arrhenius plot of the saturation island density in Figure 3.5 using relation (3.11). For the saturation regime, i.e. $\theta \approx 0.1$ ML, the term $\eta(\theta)$ corresponds to 0.2,

²Strictly speaking $\chi = 1/3$ is only exact for compact islands. For ramified islands slightly higher values have been reported [BC94]

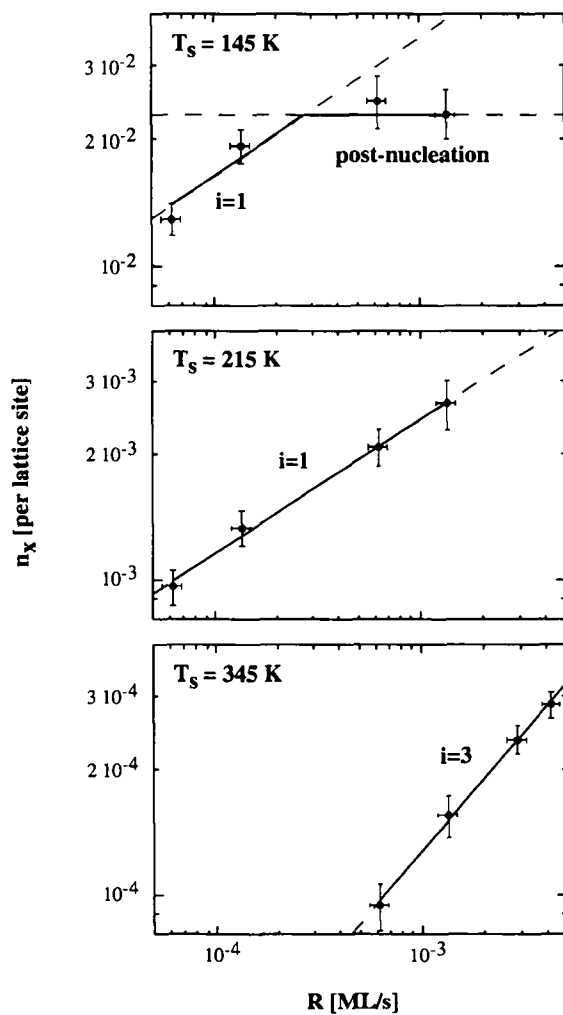


Fig. 3.6. Double-logarithmic plots of saturation island densities versus deposition flux at different growth temperatures (as indicated) and fixed coverage (0.1 ML).

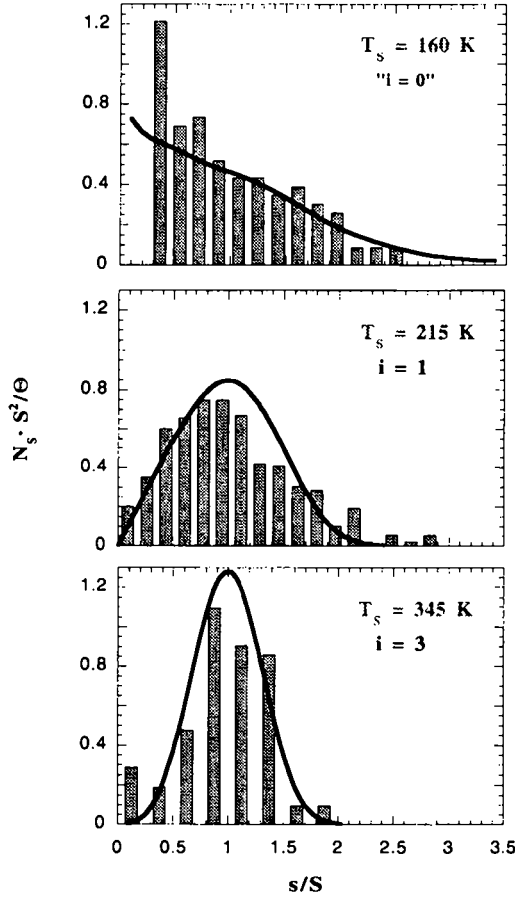


Fig. 3.7. Scaled island size distributions deduced from STM images at different substrate temperatures (deposition flux 1.5×10^{-3} ML/s). The bar diagram represents the island size distributions as obtained experimentally at the indicated temperatures, the solid line the island size distributions for the $i = 0$, $i = 1$ and $i = 3$ case according to [AF95]. At 160 K, post deposition growth is observed, i.e., the growth behaviour is not truly $i = 0$. This explains the differences between experimental and literature values.

and (3.11) can be written:

$$n_r \cong 0.2 \left(\frac{4R}{\nu_0} \right)^{\frac{1}{i+2}} \exp \left(\frac{iE_m + E_i}{(i+2)kT} \right) \quad (3.13)$$

The migration barrier and attempt frequency, E_m and ν_0 , for Cu/Ni(100) are obtained in the temperature range where the critical nucleus is one (between 160 and 320 K). The slope of the linear fit results in a migration barrier of $E_m = (0.35 \pm 0.02)$ eV. The attempt frequency is found by the intersection of the linear fit with the ordinate and yields $\nu_0 = 4 \times 10^{(11 \pm 1)}$ Hz. From the slope of the second linear fit, where $i = 3$, the binding energy of the critical nucleus (the trimer) was determined to be (0.93 ± 0.38) eV. Based on the bond counting argument already described in section 3.1.3, the dimer bond energy E_2 is half of the trimer bond energy, i.e., $E_2 = E_b = (0.46 \pm 0.19)$ eV.

As an additional check for the consistency of the foregoing analysis, one can extract the attempt frequency for single bond breaking from the intersection of the ordinate and the fit to the $i = 3$ data. The value, $\nu_0^* = 5 \times 10^{(12 \pm 2)}$ Hz, agrees within the error bars with the attempt frequency of monomer migration. If one would ignore the result from the flux dependency and the scaling behaviour ($i = 3$) and assumes $i = 2$ for substrate temperatures above 320 K, one obtains an attempt frequency of $\nu_0^* = 5 \times 10^{(15 \pm 2)}$ Hz, which is far too high, since the attempt frequencies for the different processes are of the same order of magnitude.

It is interesting to compare our experimental results to calculations performed with Effective Medium Theory (EMT) [Jac88, Sto94]. For hopping migration of copper on Ni(100), we calculate $E_m = 0.47$ eV, which is slightly higher than our experimental value; it compares well with the value of 0.45 eV calculated by Perkins and DePristo [PD94]. For the activation barrier of dimer dissociation we calculate 0.74 eV yielding a dimer bond energy of $E_b = 0.27$ eV, which is somewhat smaller than the experimental value. In view of the approximate character of EMT and the large error bar of E_b in the experiment, there is reasonable agreement.

Our results are compiled in Table 3.1, where also data of the related system Cu/Cu(100) are assembled. Our value for the migration barrier compares well with the experimental data for Cu/Cu(100). For example, Dürr *et al.* found from a LEED analysis of island separations as a

System	E_n [eV]	E_{dimer} [eV]	temperature behaviour (e.g. smallest stable cluster)	author	technique
Cu/Ni(100)	0.35 ± 0.02	0.46 ± 0.20	< 160 K Post Nucleation	our results	STM
			< 320 K Dimer	Perkins and	
	0.47 0.45	0.27	> 320 K Tetramer	DePristo [PD94]	
Cu/Cu(100)	0.36 ± 0.03	(0.06)	< 223 K Dimer	Dürr <i>et al.</i>	SPA-LEED
			> 223 K Tetramer	[ZWDL94, DWZ95]	
	0.45 0.24		> 223 K bridge hopping	Markov [Mar96]	reinterpretation of Dürr's results
			< 223 K concerted substitution		
	0.38	0.20	< 223 K Dimer	Evans and Bartelt [EB96]	reinterpretation of Dürr's data using Monte Carlo simulation
	0.4		> 223 K Tetramer	DeMiguel <i>et al.</i> [DSC'87]	
	0.39		140 \pm 5 K onset of migration	Breeman and Boerma [BB92]	low energy ion scattering, E_n from migration onset temperature
	0.28 ± 0.06		> 160 K Dimer	Ernst <i>et al.</i> [EF1.92]	
			< 160 K no adatom mobility		
	0.45	0.43		C. L. Liu [Lin94]	embedded atom

^aThe EMT code was made available to us by J. Jacobsen, K. W. Jacobsen, P. Stoltze, and J. Norskov (DTU Denmark).

Table 3.1: Experimental and theoretical findings of growth relevant parameters for the Cu/Ni(100) and Cu/Cu(100) system.

function of temperature $E_m = (0.36 \pm 0.03)$ eV [DWZ95] which is very close to our value.

Our experimental value for the dimer bond energy $E_b = (0.46 \pm 0.19)$ eV is large in relation to the migration barrier. This explains the sharp transition from $i = 1$ to $i = 3$ and the well-defined $i = 3$ regime, which is not generally expected for nucleation on square lattices [BPE95]. For Cu/Cu(100), on the other hand, Dürr *et al.* report a surprisingly small (average) dimer bond energy of 0.06 eV [DWZ95]. Based on this value, a transition from $i = 1$ to a well defined $i = 3$ regime is not expected [BPE95]. From the dependence of island separation versus flux, the authors conclude, however, that such a transition occurs [ZWDL94]. Since the value of E_b is based on this assumption, it should be interpreted with care, as has also been noticed by the authors themselves [DWZ95]. Moreover, the experimental value is too small compared with theory [LA92]. An evaluation of Dürr's data based on a Monte Carlo approach yielded a binding energy of 0.20 eV [EB96], which is a more realistic value. Nevertheless, the lateral bonding of copper on Cu(100) seems to be significantly weaker than on Ni(100).

From Field Ion Microscopy (FIM) measurements, it is known that migration of single adatoms on fcc(100) surfaces can involve exchange processes (see e.g. Pt/Pt(100) [Kel94]). This implies the question whether surface migration of Cu/Ni(100) takes place by exchange or hopping. Since Cu/Ni(100) is a heteroepitaxial system, one should find indications for exchange processes, either upon different imaging of copper and nickel atoms (the distinction of different metal atoms within alloyed surfaces by means of STM has been reported several times [CC92, SSV93, RSBK93]), or from a particular nucleation behaviour [CJ94, MB95]. Up to substrate temperatures of 400 K, there is no evidence for intermixing in the STM images, and the nucleation behaviour is in full agreement with migration by hopping on fcc(100). Above 450 K, on the other hand, the step edges appear spotmarked, indicative for the onset of alloying [Röder94, RSBK93]. Therefore, we conclude, in agreement with a theoretical study [PD94], that for Cu/Ni(100) surface migration takes place by hopping in the temperature range investigated here (100–400 K).

3.2.4 Post-deposition growth and nucleation

In Figure 3.5 the low temperature regime ($T < 160$ K) is labeled post-nucleation. Under these conditions, adatom diffusion is slow with respect to deposition, and nucleation and growth largely take place after deposition. Therefore we call this regime post-nucleation and post-growth, respectively. Post-nucleation occurs because after the deposition the sample is kept at the same temperature for STM imaging. The effect can be almost suppressed, when the sample is immediately quenched down to 30 K after deposition, because then the remaining monomers are frozen and can subsequently be imaged by STM [BHM⁺96].

Here, we summarize the experimental observations for low \mathcal{D}/R -ratios ($\mathcal{D}/R < 10^4$). First, there is a plateau in the Arrhenius plot for substrate temperatures of less than about 160 K (cp. Fig. 3.5). Second, we have also found a plateau for the rate dependency of the island density at 145 K (Fig. 3.6). The crossing of the horizontal line and the line labeled $i = 1$ in Figure 3.5 and 3.6 can in both cases be related to $\mathcal{D}/R = 5 \times 10^2$. Third, the analysis of the scaled island size distributions at 160 and 215 K results in a totally different behaviour (Fig. 3.7). At 215 K the scaled island size distribution has a maximum of 0.8 and shows clearly that the critical nucleus is a monomer [SP94, BE92, AF95]. This is consistent with the measured exponent of $\chi = 1/3$ at this temperature. At 160 K, on the other hand, the scaled island size distribution decreases monotonously in an exponential fashion as has been found for statistic growth ($i = 0$) [AF95]. Thus, post-growth results in a behaviour very similar to statistic growth, however, the mean island sizes are much larger due to monomer mobility. Statistic growth on a square lattice would result in a mean island size of 1.25 atoms at 0.1 ML [SG76], whereas we observe a mean island size of 5.5 at 160 K. At this temperature, post-growth plays the dominant role, the monomers are mainly incorporated into islands that have already formed during deposition. For lower temperatures ($T < 150$ K), post-nucleation becomes more and more important, as an essential amount of monomers forms additional nuclei after deposition. Taking account for this difference, we distinguish the post-growth and the post-nucleation regime.

These experimental findings can be compared to a rate equation analysis. In addition, the rate equation analysis allows to establish the limits between the post-growth and the post-nucleation regime, an information

which is not accessible by STM. Restricting these computations to the regime where the dimer is the smallest stable island ($i = 1$), the rate equations (3.2) and (3.3) are perfectly valid. The evaluation of capture numbers was based on the lattice approximation. The numerical results of this analysis are presented in detail in ref. [MNF⁺]; there, the rate equation results are also compared with percolation theory.

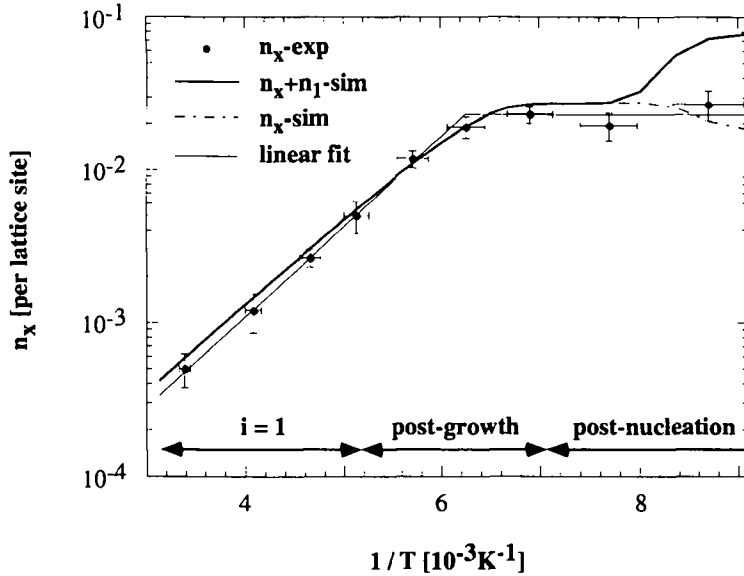


Fig. 3.8. Comparison of the Arrhenius-like behaviour of calculated and experimental island densities at 0.1 ML. The transition from dynamic nucleation (with $i = 1$) to post-growth with decreasing temperature is reasonably good reproduced by the rate equation analysis. In the post-nucleation regime the measured island densities are significantly lower than the ones expected from the calculation of stable islands n_x , which might be interpreted as an indication for transient mobility.

All experimentally observed phenomena from dynamic nucleation with $i = 1$ to post-nucleation discussed above, can qualitatively be explained by our rate equation analysis. This is demonstrated in Fig. 3.8

comparing the measured and calculated island densities as a function of $1/T$. The quantitative agreement between the experimentally observed island densities and the simulated ones is fairly good; it may be improved by an appropriate choice of capture numbers. The lattice approximation used here results in slightly higher values than the experiment, as also found by Bott *et al.* [BHM⁺96]. The solid line in Fig. 3.8 represents the calculated total island density including the monomers which exist after a wait-time of 10^4 s, whereby the dashed line shows only the stable islands, i.e., dimers and bigger ones. For the dynamic and the post-growth regime, the curves are identical. The difference between the $(n_x + n_1)$ - simulation (solid curve) and the experimental data in the post-nucleation regime suggests that atoms directly upon deposition have an enhanced mobility with respect to equilibrated adatoms at these substrate temperatures; this might be ascribed to transient mobility [EJ89].

3.2.5 Post deposition growth observed by SPA-LEED

The post deposition growth has been monitored by the observations of the full width half maximum (FWHM) of the LEED profiles of the (00) beam. In these experiments, we have chosen conditions ($R = 6 \times 10^{-3}$ ML/s, $T = 143$ K, $1/T = 7 \times 10^{-2}$ K⁻¹), where we expect the post deposition growth to be well developed. Due to experimental restrictions (profiles were recorded with the internal e-gun, and, between the closing of the shutter and the acquisition of the first spot profiles, the sample position had to be readjusted) it was not possible to obtain data immediately after the stop of depositing, but after ~ 800 s. During the SPA-LEED measurements, post growth – capture of single adatoms by existing islands – should be dominant; post nucleation was neglected in our analysis, although we could not check its influence. A coverage of $\theta \cong 0.3$ was chosen, as a lower coverage is hardly accessible by SPA-LEED.

Qualitative results The recorded scans were fitted numerically by Lorentzian like profiles (for details, see Chapter 6). All spot profiles can be described adequately by a combination of a sharp central peak and a broad shoulder (see Fig. 3.9).

While the central peak's full width at half maximum (FWHM) is time-independent, the FWHM of the broad shoulder was varied in the fit process. A typical evolution in time of the latter is shown in Fig. 3.10.

One observes a constant sharpening of the broader Lorentzian, its FWHM decays. The FWHM of the broader Lorentzian is determined by the mean island size. The sharpening demonstrates the increase of the mean island size, caused by the post deposition growth.

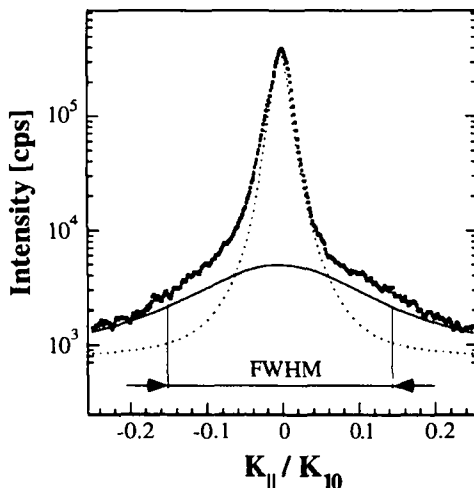


Fig. 3.9. LEED-spot profile analysis of post deposition growth. The profiles – here we display a profile of the (00) spot at an electron energy $E = 37.6$ eV – can be described as a combination of a sharp peak (broken line) and a broad shoulder (full line). The post deposition growth was monitored due to a diminution of full width at half maximum (indicated) of the broad shoulder. ($\theta = 0.32 \pm 0.02$, $R = (5.0 \pm 0.4) \times 10^{-3}$ ML/s, 3200 s after deposition stop)

Quantitative results The decay indicated in Figure 3.10 was used to quantify the post-growth phenomena by means of adatom terrace migration. At the chosen experimental temperature, the dimer is the

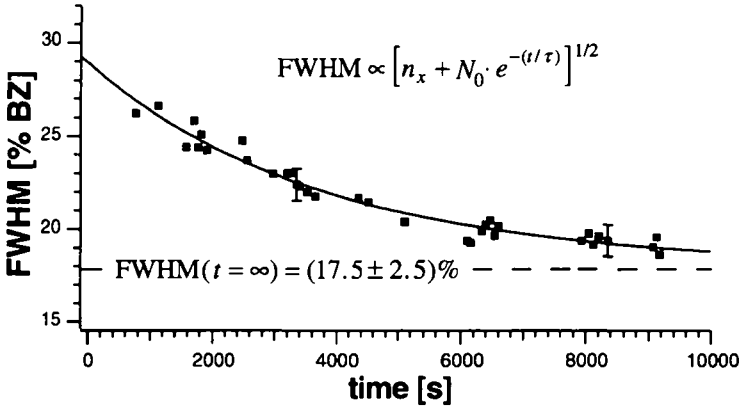


Fig. 3.10. Evolution of the FWHM of the broad Lorentzian with time and the fit of these data. ($\theta = 0.32 \pm 0.02$, $R = (5.0 \pm 0.4) \times 10^{-3}$ ML/s, electron energy $E = 37.6$ eV, $S_{Cu} = 1.8$)

smallest stable cluster and hence the rate equations (3.2) and (3.3) are perfectly valid. The terms accounting for the arrival of adatom (post deposition) and the impingement terms have to be discarded. Also, by supposing that the only process relevant for the changes in spot profiles is the incorporation of monomers into existing islands, one can neglect the nucleation and coalescence terms, and equation (3.2) writes:

$$\frac{dn_1}{dt} = -D\sigma_x n_1 n_x \quad (3.14)$$

This allows us to derive an exponential law for the decrease of the monomer density n_1 :

$$n_1(t) = N_0 \exp(-D\sigma_x n_x t) = N_0 \exp(-t/\tau) \quad (3.15)$$

The FWHM of the spot profiles is inversely proportional to the mean island diameter [LC84], hence $\text{FWHM} \propto 1/\sqrt{\bar{s}}$. Here, \bar{s} denotes the mean size of *all* islands, i.e., a monomer is considered to be an island,

too: $\bar{s} = \theta/(n_1 + n_x)$. From these expressions, one can deduce the time convolution of the FWHM,

$$\text{FWHM} \propto \left(n_x + N_0 \cdot e^{-(t/\tau)} \right)^{1/2} \quad (3.16)$$

where n_x , the density of stable islands is assumed to be constant (post growth, no post nucleation). As $1/\tau = \mathcal{D}\sigma_x n_x = \frac{1}{4}\sigma_x n_x \nu_0 \exp(-E_m/kT)$ (equation (3.15)), the migration barrier E_m can be determined from the characteristic time constant τ .

Fitting the expression (3.16) to the experimental data yields $\tau = (3200 \pm 2600)$ s. We assumed an attempt frequency $\nu_0 = 4 \times 10^{11 \pm 1} \text{ s}^{-1}$ and an error in the temperature measurement of ± 7 K. Furthermore we supposed the capture numbers to be invariant during the experiment: $\sigma_x(\theta = 0.3 \text{ ML}) = 34$ (=value based on the lattice approximation ([Ven73, Fig. 2])). Then, with $n_x = (2.3 \pm 0.2) \times 10^{-2} (\text{site})^{-1}$, one obtains a migration barrier $E_m = (0.41 \pm 0.07) \text{ eV}$. This value, averaged over a surface of $\sim 1 \text{ mm}^2$, is in excellent agreement with the STM-results.

3.3 Conclusions

Post-growth and post-nucleation, which show similarities to statistic growth, have been observed and quantitatively discussed for copper nucleation on Ni(100) for $\mathcal{D}/R < 10^4$. The post-growth and post-nucleation phenomena are not only interesting from a fundamental point of view but also of potential technological relevance since in industrial film growth deposition rates are orders of magnitudes higher. Typical growth rates in MBE (1 ML/s) are three orders of magnitude higher than in our experiments and for laser deposition experiments the rates are up to 8 orders of magnitude higher than the ones discussed here. Therefore, post-nucleation and post-growth can play an important role even at high temperatures depending on the \mathcal{D}/R ratio. We demonstrated that by the use of a simple rate equation analysis, a better understanding of the first stages of epitaxial growth on an atomic scale can be obtained.

However, such an analysis needs a starting point, i.e., an exact knowledge of the kinetic and thermodynamic quantities governing the microscopic processes during growth. The Arrhenius behaviour of the satu-

ration island density was experimentally determined; this allowed us to determine the aforementioned quantities. The analysis yielded an energy barrier for adatom terrace diffusion $E_m = 0.35 \pm 0.02$ and the binding energy $E_b = 0.46 \pm 0.20$. Also, the size of the critical nucleus i was determined. At a temperature of 320 K, an abrupt transition from $i = 1$ to $i = 3$ has been demonstrated. This is consistent with expectation (see Sect. 3.1.3), and shows nicely that for copper on Ni(100), dimer and trimer dissociation can be associated with similar energy barriers. Such particularities of the specific system have to be taken into account if one wishes to give a correct picture of the very early stages of epitaxial growth.

Chapter 4

Effects of the lattice mismatch on island shapes

The shapes of islands in epitaxial growth can vary considerably; examples range from compact forms such as droplet-shaped or squares [SPD93, HKWK95] to ramified, dendritic or fractal shapes [BRRK94, BBK⁺96, BRB⁺96, Röder94, MHBC93, HSGB91, HB92]. Especially fractal growth forms raised interest, as they are a convincing example for the universality of fractal geometry, a recent branch of mathematics.

Until now, ramified islands with dendritic or fractal shape have been observed on triangular or hexagonal but not on square lattices. This empirical observation caused Zhang *et al.* [ZCL94] to generalize the experimental findings. As the occurrence of fractal shapes is in general attributed to kinetic mechanisms associated with hindered edge diffusion, the authors classified the growth regimes that may lead to compact or fractal and dendritic shapes. On a triangular lattice the presence of two-fold coordinated edge sites substantially increases the barrier for edge diffusion and a fractal growth regime exists in an extended substrate temperature and flux range. On square lattices, only kink sites have two-fold coordination. Atoms remain edge mobile until they find such a kink

site. A growth regime generating ramified island should thus necessitate exceptionally low growth temperatures. A metal on metal system with square symmetry should always form compact islands at substrate temperatures above ~ 100 K.

4.1 STM observation

STM images of submonolayer copper films grown on Ni(100) at a substrate temperature of 345 K are shown in Figure 4.1. At low coverage, the islands are relatively small and, as expected, compact. At higher coverage, the smaller islands are still compact whereby the larger ones show a ramified shape. At even higher coverage, the islands form ramified structures which seem to have a well-defined armwidth.

Considering the arguments outlined above, this observation is surprising since compact islands are generally considered to be the most stable configuration. Kinetic arguments are not realistic at these high substrate temperatures because edge diffusion on square lattices is fast enough to produce compact islands. Nevertheless, we have checked the influence of kinetics on the island shapes by changing substrate temperature and deposition rates. Both, the change of substrate temperature and flux leads to different island densities, but, starting from a certain island size of about 500 atoms, the islands are always ramified. We have been able to obtain ramified islands at temperatures between 250 and 370 K, whereby the flux was varied between 6×10^{-5} and 3×10^{-2} ML/s. The typical coverage ranges from 0.01 to 0.5 ML. Indeed, this is an extended range of growth parameters. Note, this range includes the transition in critical nucleus from $i = 1$ to $i = 3$ [MNF⁺]. The invariance of island shapes is demonstrated in Fig 4.2. Though the growth conditions chosen in the two experiments differ drastically (substrate temperature 250 K and 345 K, respectively), one observes equivalent ramified shapes. The same is valid for changes in the deposition rate (cf. Figure 3.2 (d)). Hence, also these qualitative observations suggest that kinetics is not the reason for the ramified island shape.

(a) $\Theta = 0.01$ ML(b) $\Theta = 0.03$ ML(c) $\Theta = 0.13$ ML

Fig. 4.1. Transition from compact to ramified island shapes at submonolayer coverage: At low coverage (a), all islands are compact. With increasing coverage, the branching of the larger islands sets in (b), until, at still higher coverage (c), one only observes large ramified islands. The growth conditions remained unchanged in this experimental series ($T_s = 345$ K, $R = 1.5 \times 10^{-3}$ ML/s, mean island size \bar{s} , (a): $\bar{s} = 80 \pm 15$ atoms, (b): $\bar{s} = 180 \pm 40$ atoms, (c): $\bar{s} = 1200 \pm 200$ atoms).

We complemented our study by a quantitative analysis of island shapes. Quantities which describe the island topology have been evaluated, such as island size, perimeter and radius of gyration.

The relation between the radius of gyration r_g and the size of islands is displayed in Figure 4.3. Data concerning the topology of more than 3000 islands have been analyzed, each dot in the log-log plot represents one island. A widespread method to describe the 'compactness' of a ge-

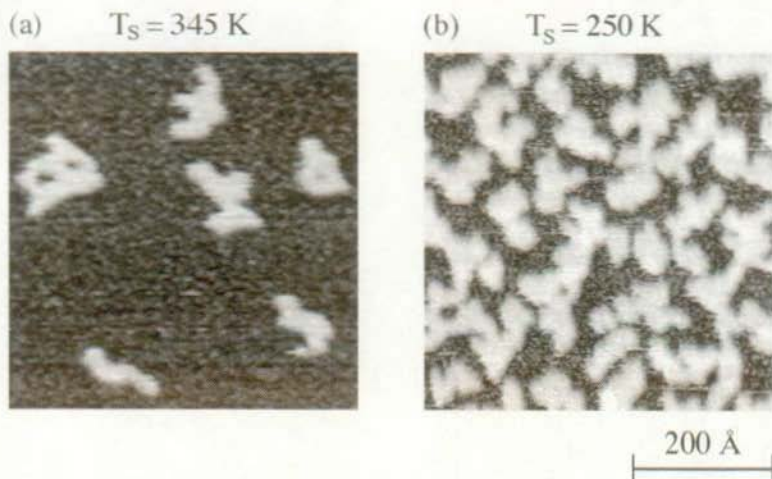


Fig. 4.2. Ramified islands grown at strongly differing growth conditions. ((a): $\theta = 0.07$ ML, $T_S = 345$ K, $R = 1.5 \times 10^{-3}$ ML/s, $\bar{s} = 440 \pm 100$; (b): $\theta = 0.5$ ML, $T_S = 250$ K, $R = 1.5 \times 10^{-3}$ ML/s), $\bar{s} = 1000 \pm 200$

ometrical object is by the determination of its Hausdorff number. The Hausdorff number (also referred to as fractal dimensionality) defines a scaling relationship between the mass or the surface area and a characteristic length. It is common practice to determine the Hausdorff number by the radius of gyration r_g according to

$$r_g \propto A^{1/H}, \quad (4.1)$$

where A is the size of the object [Mea88]. Compact two-dimensional objects such as circles or squares have a Hausdorff number of 2, 'non-compactness' leads to diminution of the Hausdorff number below 2. An evaluation of the Hausdorff number based on Fig. 4.3 yields an overall Hausdorff number close to 2 ($H = 1.91 \pm 0.02$). This is not surprising, since even heavily ramified islands adopt a rather compact form, the branched arms are separated by only narrow 'canals' (see Fig. 4.1, 4.2).

Again, we checked carefully whether the growth conditions have an influence on the islands shapes. Note: Figure 4.3 unifies the results of experiments carried out at vastly differing temperatures and growth rates and the aforementioned Hausdorff number of 1.9 is an average

value based on all these experiments. We determined the Hausdorff number as a function of growth conditions, i.e. temperature and flux. Except for statistical deviations, the Hausdorff number was found to be independent of growth conditions. The only variation we were able to detect was a slight decrease of the Hausdorff number for island sizes around 500 atoms, i.e. in the regime of transition from compact to ramified growth. However, this decrease is rather small ($H = 1.75 \pm 0.5$), and it is exclusively related to the island size, i.e. independent of growth conditions.

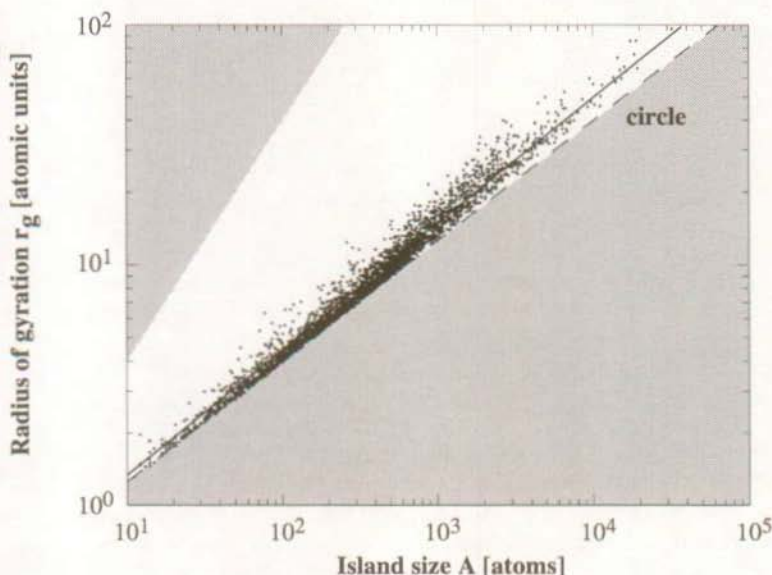


Fig. 4.3. Radius of gyration versus island size. Each dot represents one island. Grey areas indicate 'forbidden zones', i.e. a twodimensional object cannot have a Hausdorff number larger than 2 (lower part) or smaller than 1 (upper part). The full line indicates the linear fit with $H = 1.9$, the broken line the radius of gyration of a circular island ($H = 2.0$). Small islands ($A < 500$ atoms) are compact, their radius of gyration does not differ much from the one of a circular disk. Larger islands are ramified, however, in terms of radius of gyration, their form remains rather compact.

Growth conditions definitely determine the island sizes. But, concerning the island shape, deposition flux and temperature are found to be irrelevant. The only relevant parameter for the island shape is the island size. Thus, we can definitely exclude the branching of islands to be of kinetic origin. On the other hand, this allows us to use all STM images for a quantitative analysis independent of growth conditions.

4.2 Ramified islands – an equilibrium state?

Three major conclusions can be drawn from the experiments presented in the previous paragraph:

- Growth kinetics as a driving force for the island branching can definitely be ruled out.
- The island sizes have a deterministic influence on the topological quantities. For a given island size, the radius of gyration falls into a rather narrow interval.
- The qualitative observation ‘small islands are compact, large islands are ramified’ can be confirmed. In Figure 4.3 the radius of gyration of a circular island is indicated. This approximation works nicely for small islands, above a critical size (~ 500 atoms), substantial higher radii indicate the ramified island shapes.

The current models which account for non-compact island forms are based on kinetic arguments; these arguments fail to describe the observed phenomena. This caused us to query whether the assumptions upon which the aforementioned models are based are of general validity. According to these models, fractal or ramified growth shapes are metastable configurations, the thermodynamically preferred form is a compact one. This principle is correct in the case of homoeptaxy, but does not take into account the lattice mismatch between substrate and film material. In the following, we will discuss a simple concept, which explains the ramification of islands in terms of the lattice mismatch. It is motivated by the fact that on Pd(100) only compact copper islands are observed [HKWK95]. Both substrate materials, Ni(100) and Pd(100), are very similar. However, the copper layers are compressively strained

on Ni(100) and tensile strained on Pd(100). Therefore, we expect the positive misfit to play the crucial role in the branching of islands.

For a flat, defectfree, twodimensional submonolayer film, one can distinguish between two extremes: strained-pseudomorphic or relaxed-incommensurate growth. For pseudomorphic growth on a square lattice, the most stable configuration is a square. Usually, islands are at least partially relaxed, and edge atoms will be pushed away from the ideal four-fold coordination hollow site. This displacement is more pronounced for larger islands. In particular, for an island under compressive strain edge relaxation is feasible as the edge atoms are free to expand outwards.

It is likely that with increasing island size, at first corner positions will become energetically unfavourable and the islands will have a round or polygonal form. For even larger islands a ramified shape may be the most stable form. Such a ramified form is associated with a loss of intralayer binding energy, since the transition from a compact to a ramified form involves the breaking of bonds and a large number of atoms will have a reduced coordination. However, in a ramified island strain can effectively be relieved at the step edges while shifting the edge atoms only slightly away from the preferred adsorption site, i.e. the loss of interlayer binding energy is not excessively large.

That means, in the transition towards ramified growth shapes the energy gained through edge relaxation overbalances the loss of intralayer binding energy and ramified islands have a higher total binding energy. Such a transition cannot be a kinetically driven phenomenon, it must be independent on the growth parameter – substrate temperature and deposition rate – as observed experimentally.

4.3 Evaluation of ramified island shapes based on the linear chain model

The arguments mentioned above explain the experimental finding qualitatively: Islands smaller than 500 atoms are compact, larger islands adopt a ramified form. For a detailed understanding of the observed island shapes, a quantitative interpretation of the topological data is necessary. However, the transition from compact to ramified growth forms does not translate into a marked change of fractal dimensionality.

An evaluation of the perimeter \mathcal{U} , in analogy to Figure 4.3, is displayed in Figure 4.4. For the specific growth shapes in the Cu/Ni(100) system, the island perimeter \mathcal{U} is better suited to indicate differing growth topologies. The upper graph shows the raw data, each dot corresponds to one island. In the lower graph, the islands of a certain size range are averaged, and the mean values as well as the statistic error bars are displayed. Up to a critical size A^* , the island perimeter grows by the square root of the island size as expected from compact shapes such as circles and squares. Above that value, the islands grow like a linear chains of a certain width d . This width can be fitted from the raw data starting from a certain size, e.g. 400 or 1000 atoms, using an equation obtained from a linear chain. Considering a simple model of square atoms on a square lattice, the perimeter \mathcal{U} is determined by the islandsize A according to

$$\mathcal{U} = 2 \left(\frac{A}{d} + d \right). \quad (4.2)$$

Because the relation between \mathcal{U} and A is given by the experiment, the armwidth d is the only fit parameter. Using the data of the island sizes above 1000 atoms, we obtain $d = (21.98 \pm 0.25)$ atoms. For island sizes above 400 atoms, the obtained value is almost the same: $d = (21.87 \pm 0.18)$ atoms. That means, the armwidth corresponds to (22 ± 1) atoms, and the critical island size found by the linear chain model equals (480 ± 20) atoms.

An armwidth of 22 atoms is a reasonable value. The edge atoms are displaced from the ideal four fold coordinate hollow site by $22 \cdot \frac{1}{2} \cdot 2.6 \% \cong 1/4$ next neighbour distances for a fully relaxed adlayer. The armwidth is also below the critical island size for the occurrence of the protruding stripes, a strain relief mechanism which is operative at higher coverages and will be discussed in Chapter 5.

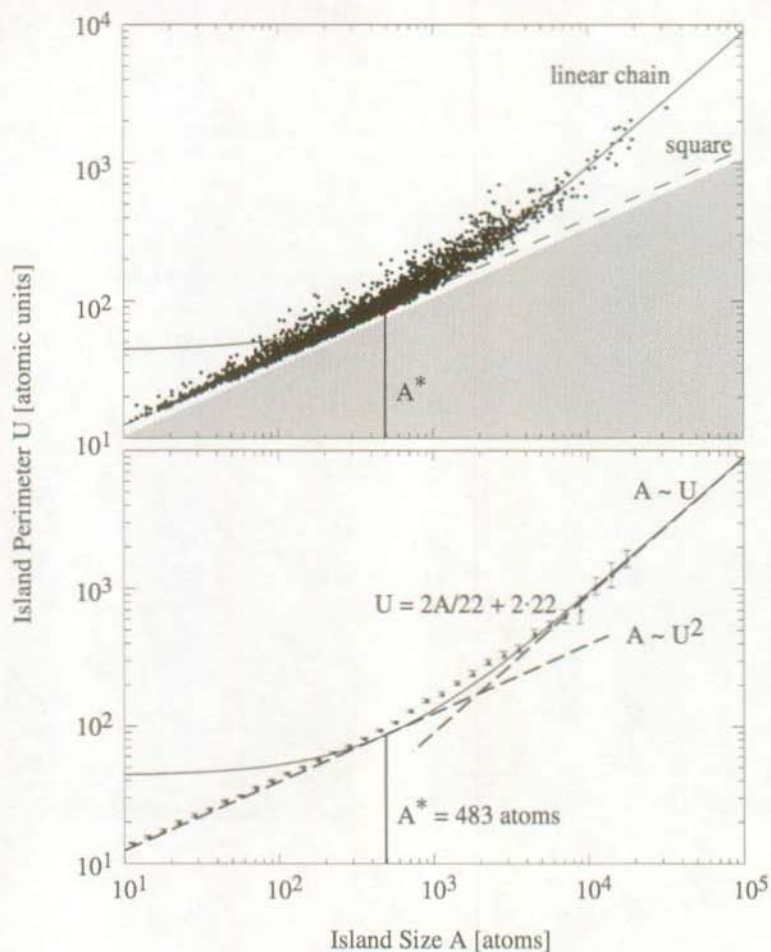


Fig. 4.4. Perimeter versus island size: In the upper graph, the raw data are presented. At the bottom, the graph shows the average perimeter as a result of a logarithmic binning. The dashed line indicates the perimeter of a square, the full line represents the evolution according to equation (4.2). The parameter d , the width of the chain, was determined by numerically fitting the curve to the data.

4.4 Annihilation of ramified growth shapes by annealing

Ramified islands occur in a wide temperature range. However, upon annealing of the sample at temperatures above 450 K the ramified islands become compact and the step edges straight (see Fig. 4.5). Step edges and islands appear spotmarked, indicative for the onset of alloying [RSBK93]. The intermixing caused by the alloy formation significantly reduces the compressive strain of the islands, and the island change their shape to the thermodynamical stable compact form. After annealing the island diameter is much larger than the formerly observed armwidth of 22 atoms.

Growth at 345 K



Annealed to 450 K



500 Å

Fig. 4.5. STM images of a submonolayer copper film on Ni(100) before and after annealing to 450 K ($T_s = 345$ K, $R = 1.5 \times 10^{-3}$ ML/s, $\theta = 0.04$ ML). Both islands and step edges change their shape and appear spotted after annealing, which indicates the onset of alloying.

4.5 Conclusion

The occurrence of ramified island shapes could be clearly attributed to the compressive strain which is inherent to the adlayer even at submonolayer coverages. The lateral edge relaxation of copper islands on Ni(100) results in a transition from compact to ramified islands at a critical size of 500 atoms. The larger non-compact islands are characterized by an armwidth of 22 atoms. The ramified island shapes are not caused by kinetic effects.

The DLA (=diffusion limited aggregation) model is such a kinetic model and explains the formation of fractals by hindered edge diffusion and a hit-and-stick mechanism. It is not valid in the copper on Ni(100) system and monomer diffusion at the step edges is active in the whole temperature range investigated. Fractal growth form can also be generated by a second mechanism, cluster-cluster-aggregation (CCA). The CCA mechanism depends on clusters to be mobile. We did extensive experimental series to detect cluster movements, but such a cluster movement was never observed.

DLA and CCA produce agglomerates whose Hausdorff number is known, $H = 1.7$ and $H = 1.45$,¹ respectively [Mea88]. These values can not be reconciliated with the values obtained by our quantitative analysis. Also, in the case of a fractal, the Hausdorff number will be independent of the 'characteristic' length used for its evaluation. We demonstrated that the use of the radius of gyration and the perimeter yields two different Hausdorff numbers, thus the islands are no fractals.

Ramified islands only occur in the submonolayer range. It is interesting to compare islands in the first monolayer with the ones formed during the building-up of second or higher layers (see Fig. 5.3). The first monolayer relieves strain by a network of defects (see Chapter 5), accordingly, islands which nucleate on top of the first monolayer will be considerably less strained than islands on the substrate. This results in compact, rectangular island shapes, as one would expect for a square lattice.

¹Here, we list only the Hausdorff numbers for 2d fractals

Chapter 5

Strain relief by internal faceting – STM study

5.1 Introduction

Copper has been reported to grow on Ni(100) in a well defined layer-by-layer mode [CJ75, CCV⁺86a]. The lattice mismatch m of +2.6 % is relatively small, but not negligible, and the copper film is compressively strained. What is the effect of strain on growth morphology? Which mechanism is possible for strain relief? Is there any dependence between strain relief and growth mode? These are questions to be solved.

One generally accepted way to explain and quantify the effects of strain in heteroepitaxial growth are continuum models. In these models – based on an approach originally proposed by Frenkel and Kontorova [FK39] – the adlayer is supposed to remain locked to the substrate up to a finite critical thickness h_c [FvdM49, JKW67, Bal70, MC70, BZ86]. For $h \leq h_c$ the film grows essentially pseudomorphic. For a thickness $h > h_c$ strain is relieved by formation of misfit dislocations and associated lattice relaxation. Eventually, the film will adopt its bulk geometry. For typical metal-metal systems, h_c is found to vary from below 1 Å ($|m| > 10\%$) up to 10-200 Å for small misfits ($|m| \leq 2\%$) [JKW67].

However, this model has recently been reported to fail in the description of hexagonal closed packed metal interfaces [BRBK94b, GVHB95,

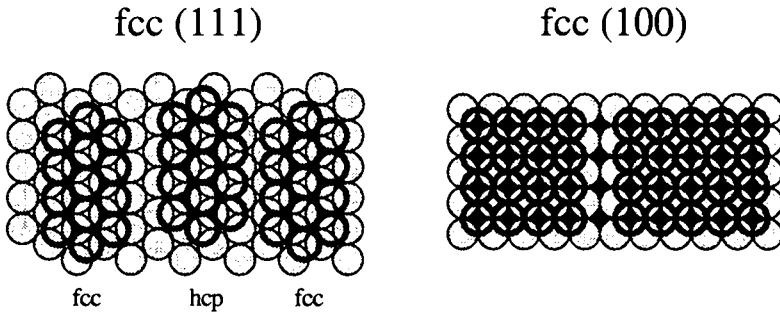


Fig. 5.1. Comparison of hexagonal surfaces (e.g. fcc(111)) and square surfaces (e.g. fcc(100)). On a hexagonal surface, two types of domains – adatoms are either placed in fcc or in hcp sites – can coexist. Strain is relieved at the domainwalls without excessive loss in binding energy. On fcc(100), all hollow sites are symmetrically equivalent and a similar strain relief mechanism is not possible.

MSB95, CH95]. The continuum model ignores any atomic details of the interface structure and, for explaining microscopic phenomena, uses quantities which are only valid on a macroscopic scale. On fcc(111) surfaces, two differing adsorption sites with similar adsorption energy exist, fcc and hcp (hexagonal closed packed) (see Fig 5.1(a)). Due to this particularity of fcc(111), strain can be accommodated easily by the introduction of fcc-hcp stacking faults: Domains of fcc and hcp stacking may coexist, at the boundary between these domains, adatoms may relax laterally without excessive loss of binding energy. The low energy cost for the formation of misfit dislocations essentially drops h_c to zero or just to the first monolayer [BRBK94b, GVHB95, MSB95, CH95].

On the other hand, such an fcc-hcp stacking fault-mechanism is symmetrically impossible at square interfaces (see Fig 5.1(b)). For these interfaces many experimental studies have been reported which seem to be in agreement with the predictions of the continuum model [Mat75]. In particular, for the copper on Ni(100) system, the continuum model predicts a critical thickness h_c of $11\text{--}17 \text{ \AA} \cong 6\text{--}10 \text{ ML}$ [JKW67]. An Auger electron diffraction study [CCV⁺86b] seemed to provide quan-

titative support of the continuum model and the measured data was explained by postulating a critical thickness h_c of 14.8 Å.

5.2 Stripe pattern observed by STM

The growth of copper on Ni(100) at 350 K is characterized in Figure 5.2 and 5.3. As mentioned, other studies of the copper growth on Ni(100) effected by TEM (=transmission electron microscopy) and AES [CJ75] or by Auger-electron diffraction [CCV⁻86a] indicate Frank-van der Merwe growth. The STM measurements confirm this result, the copper film indeed builds up in layer-by-layer. STM offers the advantage to show the growth morphology directly, no indirect analysis (e.g. interpretations in Auger electron spectroscopy involve assumptions about the length of the mean free path) is needed.

For the coverage range between 1 and 18 ML, the most striking surface feature is a network of protruding stripes. These networks are shown in Figures 5.2 and 5.3. The height of the stripes corresponds to about one third of the step height. Already for the submonolayer coverages ($\theta \cong 0.2$ ML), these stripes appear, crossing islands which are larger than 60–80 Å (see Fig. 5.2 (a)). Apparently, there is a minimum island size for stripe formation. Once the islands get bigger than 60–80 Å, there is a high probability for stripes to form. At monolayer coverage, the whole surface is covered by a network of stripes (Fig. 5.2 (b) and (c)). The stripes are all running along $\langle 110 \rangle$ with equal probability for the two orthogonal domains, as can be deduced by the fact that their preferred orientation is parallel to the step edges. For step edges on fcc(100), the $\langle 110 \rangle$ orientation is the most favorable; this general rule has been confirmed for the Cu(100) [LA92] and the Ni(100) [KGNPB93] surface.

At monolayer coverage all stripes have a width of (5.5 ± 1.0) Å which is the typical STM-imaging width of a single atomic chain: Due to size effects, STM usually overestimates the extension of objects protruding from metal surfaces. For example, monatomic copper chains are usually imaged with a width of 5–8 Å [BHF⁺94]. That means, the measured value of 5.5 Å corresponds to the size of a single atom, and the observed stripes are exactly one atom ($=2.55$ Å) in width. Stripes shorter than 20 Å are not observed.

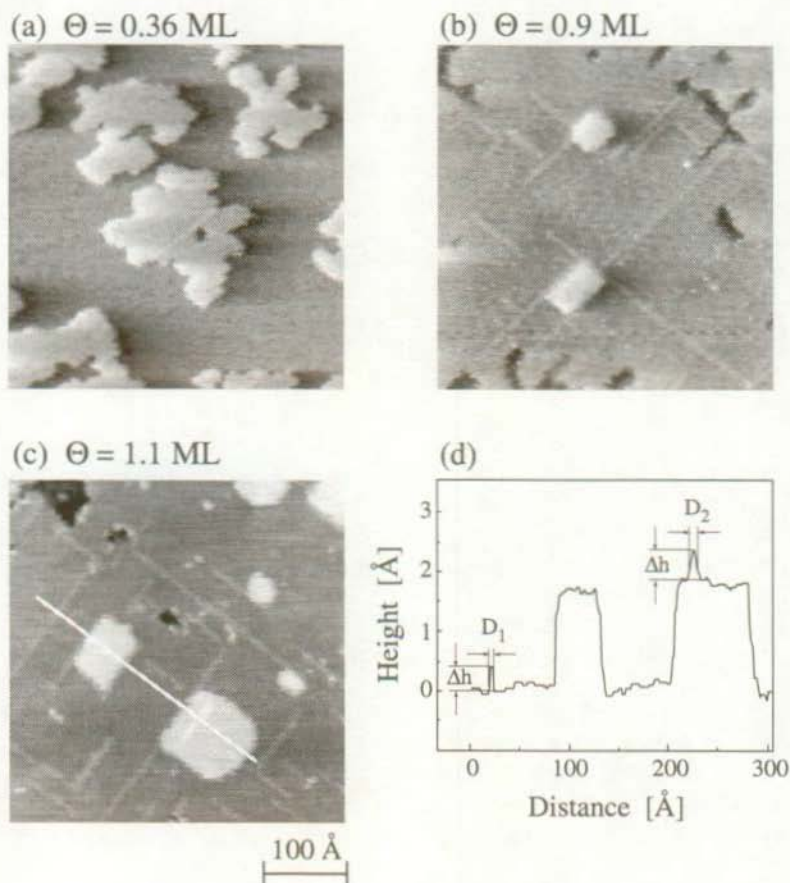
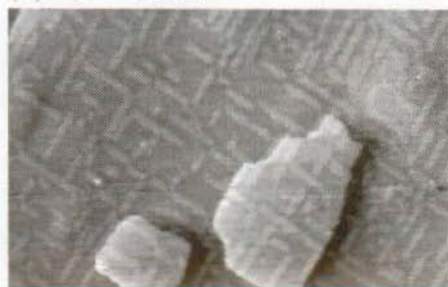


Fig. 5.2. The growth of copper on Ni(100) up to completion of the first monolayer. The substrate temperature was 350 K and the deposition rate was 1.5×10^{-3} ML/s. (a) $\theta = 0.36$ ML, (b) $\theta = 0.9$ ML, (c) $\theta = 1.1$ ML and (d) STM line scan indicated in (c).

(a) $\Theta = 1$ ML



(b) $\Theta = 6$ ML



(c) $\Theta = 11$ ML



250 Å

Fig. 5.3. Evolution of the strain induced stripe pattern at the surface of copper films of various thicknesses (1–11 ML) on Ni(100) observed by STM. The substrate temperature was 350 K and the deposition rate was 1.5×10^{-3} ML/s.

This pattern is maintained up to coverages of about 20 ML (see Fig. 5.3), only the width of the stripes increases stepwise with coverage. The average length, the density and the height of the stripes, however, remain constant above monolayer coverage. There is a further important feature of the stripe pattern: Stripes do not cross each other or coalesce, as demonstrated in all STM images shown.

5.3 Internal faceting

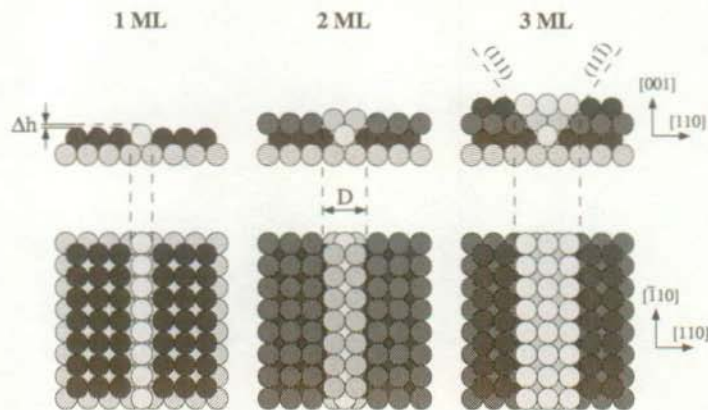


Fig. 5.4. The *internal {111} faceting model* describing the appearance of the protruding stripes at the Cu/Ni(100) interface. The Figure shows the side view and the top view for the coverages of 1, 2 and 3 ML. The shaded circles represent the substrate atoms (Nickel). The "dark atoms" (copper) are placed at the 4-fold hollow sites in the pseudomorphic geometry. The "light atoms" (copper) form the stripes and are placed at the 2-fold bridge sites in the first layer. As indicated for the coverage of 3 ML, {111} facets are formed along the stripes.

In the following, a model is discussed which accounts for the experimental observations. It is motivated by the fact that the compressive strain at fcc(100) is highest in the close-packed $\langle 110 \rangle$ direction. Therefore, intuitively it could be expected that chains of atoms are squeezed out from

the adlayer and create protruding stripes. Due to the square symmetry, these stripes have to form with equal probability in both directions $\{110\}$. The simplest way to generate such stripes is to shift copper atoms from their four-fold hollow site to the two-fold bridge site (see Fig. 5.4, coverage 1 ML). Such a bridge site atom has a reduced number of nearest neighbours in the substrate but it gains binding energy in the adlayer. There are two nearest neighbours below and, in addition, four lateral neighbours with a binding length which is only about 10 % larger. Since the protruding atoms are staggered vis-a-vis the adjacent rows, they gain lateral freedom of expansion and the film can partially relieve its strain. Obviously, this lateral freedom of expansion is overbalancing the lowered binding energy. The growth of the second layer on top of the protruding stripes leads to the formation of two atom wide chains. In the third layer, protruding stripes are three atoms wide, and so on. Consequently, the stripes, formed in the first layer, give rise to V-shaped structures in the film. Figure 5.4 shows the generation and the growth of the protruding stripes up to a coverage of 3 monolayers. The height Δh is constant for all coverages. The width D depends on the coverage, i.e., for one monolayer the stripes are exactly one atom wide, for two monolayers two atoms and so on. The stripe atoms (light colored) can relieve strain at least perpendicular to the stripes, while the atoms, which are placed in between the stripes (dark colored atoms), are expected to grow essentially pseudomorphic. However, close to the stripe boundary, these atoms are allowed to relax partially, as will be discussed in detail later (see Section 5.9).

In this model, the density of the stripes, their mean length and their length distribution is determined by the monolayer configuration. The subsequent growth stabilizes the pattern of stripes by the formation of internal $\{111\}$ facets along the stripes and $\{110\}$ facets at both ends. This is energetically favorable because the strain relaxation takes place by the formation of the highly stable close-packed $\{111\}$ facets.

An important experimental observation is the fact that stripes neither cross nor coalesce at all coverages below 18 ML. This behaviour is easy to understand in the internal faceting model. There are two domains of bridge sites on the square fcc(100) surface depending on the direction of the stripes. At their potential junction, two orthogonal stripes are always separated by $1/\sqrt{2}$ of a lattice constant (i.e. $1/2$ nearest neighbor

distance) rendering crossing impossible. Coalescence is also unlikely as the distance between two parallel stripes is given by the lattice constant of the nickel substrate and the merging of two stripes would block further transverse relaxation. Therefore, at higher coverages one can find neighboring parallel stripes which have a smaller width than the other stripes at the same image (not shown here).

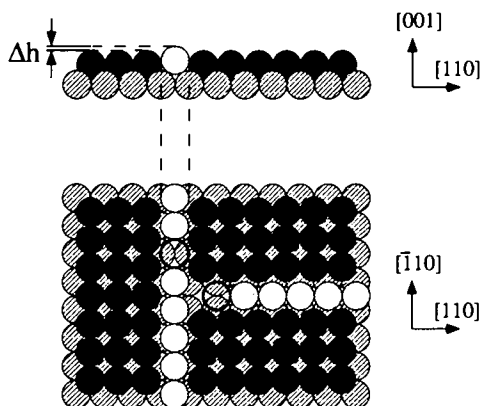


Fig. 5.5. Stripes never cross: Depending in which of the two equivalent $\langle 110 \rangle$ directions the stripes run, they occupy bridges sites which belong to one domain. At a possible junction, two orthogonal stripes are always separated by $1/2$ nearest neighbour distance, and there is no energetically favorable way to make crossing of stripes possible.

The *internal $\{111\}$ faceting model* is in quantitative agreement with the experimental observations. This is demonstrated in Figures 5.6 and 5.7 summarizing the quantitative data analysis of the stripe pattern as a function of film thickness. The first graph shows clearly that the height of the stripes is constant for all coverages. The STM measurements yield a height $\Delta h = (0.6 \pm 0.1) \text{ \AA}$. Considering the most simple case of a hard sphere model, one obtains $\Delta h = 0.4 \text{ \AA}$ for the growth of copper on nickel, which is in fair agreement with the STM results. The linear dependency of the width of the stripes on the coverage is demonstrated in the second graph of Figure 5.6. The horizontal lines indicate

the stepwise growth of the width D as expected from our model. This behaviour is also evident in the STM line scan shown in Figure 5.2. In crossing a step edge, going from one copper monolayer to the second copper layer, it is observed that the stripes are exactly one atom wider on the bilayer than on the monolayer. It should be noticed that we have plotted corrected stripe widths in Figure 5.6, taking into account the finite imaging width of the STM tip [BHF⁺94].

For coverages between 1 and 18 ML the density of stripes ρ is constant, $(8.0 \pm 1.4) \times 10^{-4}$ per substrate atom, independent of film thickness (see Fig. 5.7(a)). In the submonolayer range a critical island size for formation of stripes exists which is about 30 atomic distances ($\cong 60$ –80 Å). The first islands reach this size at coverages of ~ 0.2 ML. With increasing coverage more and more islands attain the critical size and more stripes are formed, finally saturating at monolayer coverage. It is likely, that above this critical size, relaxation at the island step edges is no longer sufficient for the strain relief of the islands (see Chapter 4), and internal faceting sets in.

Above monolayer coverage the mean length of the stripes \bar{s} remains constant, (70 ± 10) Å, independent of film thickness (Fig. 5.7(b)). This value corresponds to (28 ± 4) atoms. As the density ρ and the mean length \bar{s} of stripes are constant, and the width D increases linearly, the fraction of the surface covered by stripes ϑ_s increases linearly with film thickness θ .

The quantitative analysis of the images reveals that the density of the stripes as well as the length distribution are determined by the monolayer configuration. In Figure 5.8 we plot an example of the measured length distribution of the monolayer copper film. The distribution of stripe lengths can be described by the exponential law (see full line in Fig. 5.8)

$$N_s(s) = \frac{\rho}{\bar{s}} \exp\left(-\frac{s - s_{\min}}{\bar{s}}\right) \quad (5.1)$$

ρ is the density of the stripes and \bar{s} is their average length. For the minimum stripe length s_{\min} we have chosen 10 atoms according to the experimental data in Figure 5.8.

Stripes which are shorter than 8 atoms seem to be energetically unstable and have not been observed. Longer stripes are more stable. However, they are less frequent due to geometric restrictions: The stripes

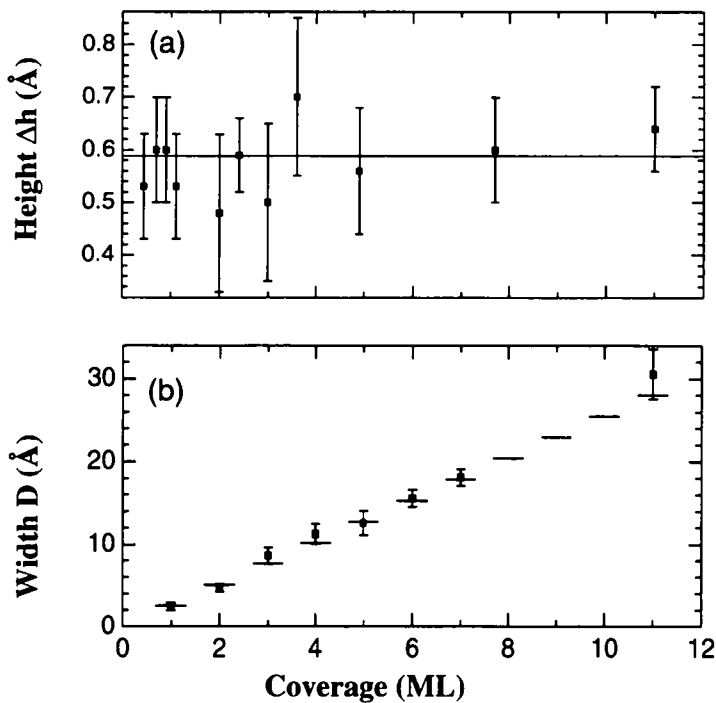


Fig. 5.6. Quantitative analysis of the pattern of the stripes observed on Cu/Ni(100). Plotted are the height Δh (a) and the width D (b), as a function of copper coverage.

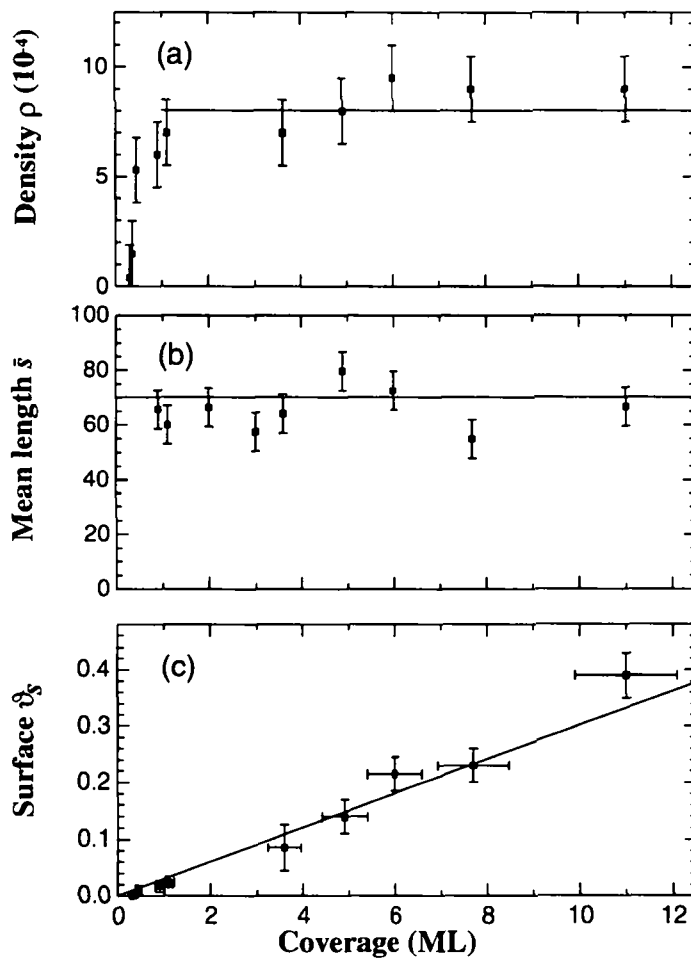


Fig. 5.7. Quantitative analysis of the pattern of the stripes observed on Cu/Ni(100). Plotted are the density ρ (a), the average length \bar{s} (b) and the fraction of the surface covered by stripes ϑ_s (c) as a function of copper coverage.

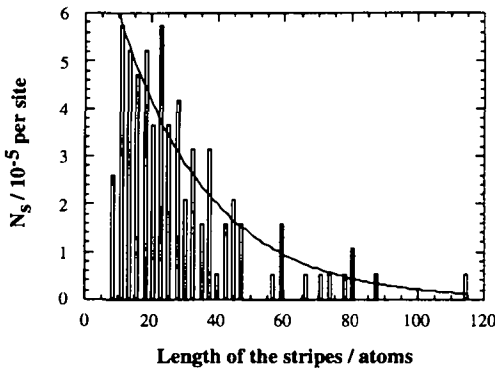


Fig. 5.8. Length distribution of the stripes (raw data). The solid line represents the exponential distribution, whereby an average length of 27 atoms, a minimal length of 10 atoms and a density of the stripes of 6.8×10^{-4} (lattice site) $^{-1}$ are assumed.

have to occur with equal probability in $[-110]$ and $[110]$ direction – otherwise the relief of strain would be inhomogenous – and the crossing of orthogonal stripes is impossible. The longer the stripes are, the more difficult it is to accommodate them in the resulting stripe network.

The density of the stripes, their mean length and the exponential length distribution do not markedly vary by the change of the deposition rate (10^{-3} – 10^{-2} ML/s), substrate temperature (between 200 and 400 K) or coverage (1–17 ML). The only noticeable changes in the adlayer morphology are correlated with the onset of alloy formation at substrate temperatures $T_s > 400$ K. These quantities and the exponential distribution function as it is shown in Figure 5.8 seem to be of universal character. Therefore, we conclude that the formation of stripes is essentially determined by the strain due to the lattice mismatch and not by the growth kinetics.

5.4 Strain relief by stacking faults

Recently, Henzler *et al.* [HHMW95] proposed a strain relief model to explain the results from a LEED study of thin potassium chloride films on NaCl(100). KCl/NaCl(100) is insofar comparable to Cu/Ni(100), as the surface is fcc(100) and the adlayer is compressively strained; the misfit is 11.7 %. The authors formulated their model in terms of stacking faults, the resulting film structure resembles closely the one obtained by the internal faceting model. Strain relief is effected by the formation of V-shaped defects. Paired stacking faults of opposite inclination – one along (111), the other along (11 $\bar{1}$) – define the two sides of the ‘V’. The pairing of stacking faults with opposite inclination assures the planar growth of the (100) surface.

The stacking fault model is a special case of the internal faceting model, where the adlayer is supposed to be perfectly relaxed. The internal faceting model makes no prediction about residual strain. In the regions between the stripes, residual strain may be accommodated. According to Henzler *al.* [HHMW95], the stacking faults define the position of the stripe atoms exactly, which leads to a stripe height of 1/3 step height.

If one allows the atoms in the stripes to relax slightly from the initial positions, one may formulate the internal faceting model in terms of stacking faults. In this terminology, each close-packed facet plane corresponds to an inclined fault along (111). The relaxation leads to a lowered stripe height, the stripe height corresponds to the difference in height between an atom on a bridge and an atom in a hollow site, namely $\sqrt{3/2} - 1 \cong 1/4$ step height.

It has been proposed [HHMW95], that Cu/Ni(100) is more adequately described by the stacking fault model. We are convinced that this is not the case. The following points show the failure of the stacking fault model:

- Henzler *et al.* deduce a mean distance between the V-shaped defects of $n = 1/(3m) - 2/3$ atoms, where m is the system's misfit. In the case of the Cu/Ni(100) system, this expression yields a stripe density of $\rho^* \approx 0.15 \text{ (site)}^{-1}$, which is clearly too high ($\rho_{\text{experiment}} = (8.0 \pm 1.6) \times 10^{-4} \text{ (site)}^{-1}$). In other words: The observed stripe density can – according to Henzlers model – be found

in a system with $\sim 0.65\%$ misfit, not in the copper on Ni(100) system (misfit $m = 2.5\%$).

- Though the STM-data yield a stripe height of $1/3$ step height which could be in agreement with Henzler's model, more precise measurements using SPA-LEED (see Chap. 6) revealed a stripe height of (0.235 ± 0.010) step height, which is in agreement with the internal faceting model, but not with Henzler's model.
- Auger electron diffraction data can be readily explained by the internal faceting model (see next section). The data indicate that with increasing coverage, the relaxation of the topmost layers increases. Such an effect cannot be explained by Henzler's model, since it supposes the film to be totally relaxed even at low coverage.

Due to the ionic nature of the binding, KCl/NaCl(100) differs from Cu/Ni(100) in its mechanical properties. These may cause a slightly differing strain relief mechanism and, in this case, it seems to be correct to apply the stacking fault model.

5.5 Interpretation of the Auger Electron Diffraction data of Chambers et al. [CCV⁺86a] by internal faceting

The growth of thin copper films on Ni(100) has been studied by Chambers *et al.* using Auger Electron Diffraction (AED). From these data, Chambers *et al.* were able to derive the transverse lattice expansion as function of coverage: Let \bar{h} denote the average lattice constant perpendicular to the overlayer, and b be the lattice constant in the plane of the interface. Their ratio \bar{h}/b defines the transverse lattice expansion. The authors compared these data with the continuum model of Matthews [MC70], which predicts a critical thickness of $h_c = 14.8 \text{ \AA} \cong 8 \text{ ML}$. Up to this thickness copper should grow pseudomorphically. Only at coverages above 8 ML, the film is expected to relax spontaneously, e.g., by the formation of bulk dislocations. In terms of the continuum model, the transverse lattice expansion \bar{h}/b must have a constant value for film thicknesses below the critical values $h_c \cong 8 \text{ ML}$.

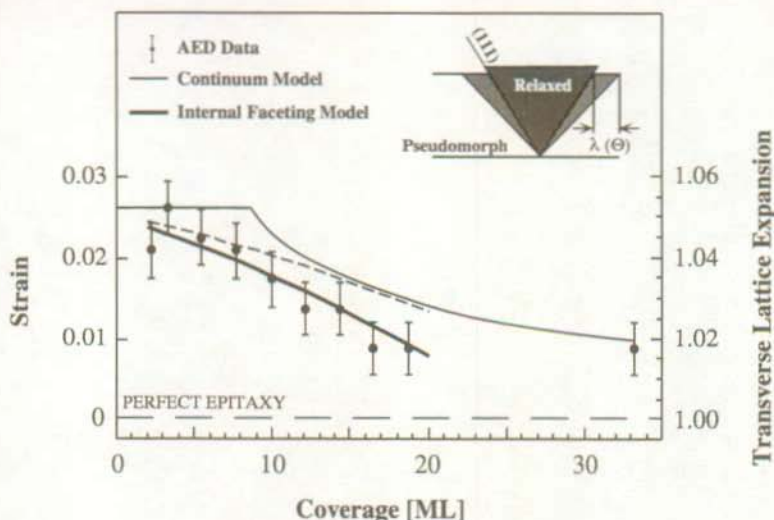


Fig. 5.9. Comparison of the *internal* {111} faceting model (thick solid and dashed line) with the Auger electron diffraction data of Chambers *et al.* (filled circle). Dashed line – only copper in the stripes is fully relaxed. Thick solid line – copper in the stripe and close to the stripe boundary is relaxed ($\lambda = 0.2\theta$).

At higher coverages, \bar{h}/b decreases due to the introduction of strain relieving defects. The expected curve according to the continuum model and the experimental AED data are displayed in Figure 5.9 (thin line and filled circle, respectively). Chambers *et al.* interpreted their experimental data as a confirmation of the continuum model. Among others, they derived a value for the atomic volume of the copper atoms in the pseudomorphic regime almost identical to the bulk phase value.

But, the internal (111) faceting model describes the AED-data much better:

Note, the transverse lattice expansion \bar{h}/b obtained by Chambers *et al.* is exactly the average value of the lattice spacing. Based on the internal faceting model and the STM data, we derived the average value

of transverse lattice expansion. Firstly, we assume the stripe atoms to be fully relaxed and the atoms between the stripes to grow pseudomorphically. Consequently, two different values of vertical spacing, h_s and h_p , were introduced. In the fully relaxed regions between the stripes, the transverse lattice expansion is unity and h_s is equal to the bulk value. For h_p , the horizontal spacing in the pseudomorphic regions, a value similar to the one obtained by Chambers *et al.* at low coverages was chosen. The fraction of the relaxed stripe volume is determined by adding up the stripe coverage in the individual layers as determined by the measurements shown in Figure 5.7(c). The relative weight of the individual layers for the AED experiment has been accounted for by the simple ansatz

$$I = I_0 \exp(-\theta/\theta_0) \quad (5.2)$$

using an reasonable attenuation factor for copper of $\theta_0 = 7$ ML [SD79]. The result is indicated by the dashed line in Figure 5.9. For lower coverages, the result agrees well with experimental data. At higher coverages, however, the experimental data suggest that the amount of strain relief is considerably higher than given by our simple ansatz.

Apparently, the copper close to the stripe boundary is not perfectly pseudomorphic but partially relaxed. One can assume (see the inset in Fig. 5.9) that an additional relaxation at the stripe boundary, $\lambda(\theta)$, depends linearly with coverage. By supposing $\lambda(\theta) = 0.2 * \theta$ (in atomic distances), one obtains the thick solid line in Figure 5.9 which is in excellent agreement with the AED-data of Chambers *et al.*¹ This implies that most of the copper between the stripes is pseudomorphic and the film relieves its strain gradually in a layer-by-layer fashion.

It is noteworthy to mention that our model also explains the Moiré fringes seen many years ago in transmission electron micrographs of 3 ML copper films on Ni(100) [CJ75], which until now were not understood [CCV⁺86a]. The copper in the stripes is relaxed while the surrounding copper matrix is essentially pseudomorphic with the nickel substrate. This difference in lattice structure between relaxed copper on

¹The attenuation factor $\theta_0 = 7$ ML is not a highly precise value. Using an attenuation factor $\theta_0 = 1.5$ ML, one can mimic the AED data without allowing for an additional relaxation at the stripe boundary (i.e. $\lambda(\theta) = 0$), but such an attenuation factor is not realistic. Assuming θ_0 to be imprecise by ± 2 ML, one obtains an additional relaxation of $\lambda = (0.20 \pm 0.05) * \theta$

one hand and pseudomorphic copper and nickel substrate on the other hand naturally explains the appearance of Moiré fringes in the TEM images.

5.6 Strain relief by a dislocation network

The internal $\{111\}$ faceting mechanism provides an efficient strain relief at intermediate coverages. However, this strain relief does not work at infinitum, and above a certain coverage h^* , strain can only be relieved in a different way. (A discussion on the exact value of h^* will be given in Chapter 7.) Figure 5.10 shows the morphology for a 24 ML copper

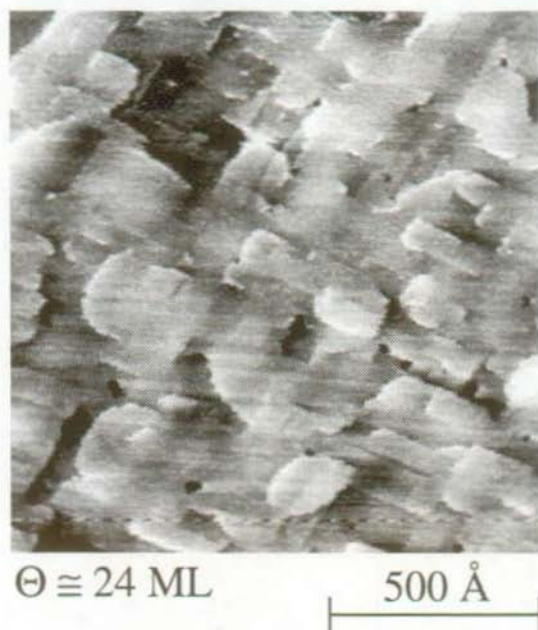


Fig. 5.10. STM image showing the morphology of a 24 ML copper film. At these coverages, the compressive strain leads to the formation of a dislocation network. ($T_s = 350$ K, $R = 3 \times 10^{-3}$ ML/s)

film. According to the internal faceting model, at such a coverage three quarters of the surface should be covered by relaxed stripes, as can be easily extrapolated from the data in Fig. 5.7(c). This is not the case: One observes relatively small, tilted, atomic flat terraces, giving raise to a dislocation network. At these high coverages, neighboring as well as orthogonal stripes merge and thereby form the dislocations.

5.7 Conclusion

The STM study shows that continuum models fail to describe the strain relief scenario in the copper heteroepitaxy on Ni(100). In fact, pseudomorphic growth has only been observed for small islands (< 1000 atoms) where strain can be partially released at step edges. The STM experiments show directly the formation of strain relieving defects starting well below monolayer coverage. From the moment the first stripes have been formed onwards, the growth cannot be considered as purely pseudomorphic.

The failure of continuum models to account for the experimental observations is due to the fact that these models do not take into consideration microscopic details of the surface structure.

We are convinced that this failure is not the exception, and that the internal $\{111\}$ faceting model is valid also for other interface systems. It should be applicable to interfaces with non-covalent bonding, i.e. metals, ionic or van der Waals-bonded crystals. The directional bonding at semiconductor interfaces usually results in an open and more complex structure. For example, the V-shaped defects in epitaxial germanium layers grown on Si(001) in the presence of arsenic observed by LeGoues *et al.* [LCT89] using high-resolution transmission electron microscopy are also strain induced and bear similarities to the defect structures based on the internal faceting model. The structure of the V-defects is, however, fundamentally different due to the covalent nature of the Ge-bonding. STM measurements of germanium growth on As-terminated Si(100) by Jusko *et al.* [JKP⁺92] do not provide any evidence for protrusion stripes or the characteristic layer-by-layer variation of the defect structures as seen in the case of the internal faceting mechanism.

Chapter 6

Strain relief by internal faceting – SPA-LEED study

6.1 Introduction

The information gained by STM offer a comprehensive picture of the strain scenario in thin films of copper on Ni(100); the use of this technique allowed us to reveal a novel strain relief mechanism – internal {111} faceting – and to characterize the resulting thin film morphology quantitatively. However, we decided to extent the studies by the use of second technique, SPA-LEED. This reciprocal space technique allows to determine average quantities such as the stripe density ρ and stripe width D with high accuracy. In addition, this technique is well suited for measuring precisely the vertical spacing in the surface topography, i.e., in our case, the height of the stripes Δh . This is particularly important, since STM images represent the electronic structure of a surface which is not necessarily equivalent to the atom position. One prominent example for the difficulties of STM height measurements is the imaging of silver islands on the Pt(111) surface [RSBK93, Röder94]. Although the atomic

size of silver with 2.89 Å is only 0.12 Å larger than that of platinum, a silver island is imaged 0.6 Å higher than a corresponding platinum island on the Pt(111) surface. For copper on Ni(100), we observed the same effect: Chambers *et al.* reported a vertical spacing of 1.855 ± 0.015 Å for copper grown pseudomorphically on Ni(100), i.e. the height difference between copper and nickel deposits should be around 0.055 Å. However, STM yields a height difference of (0.70 ± 0.25) Å, which is significantly higher. Again, this difference can be explained only by electronic contributions.

In the SPA-LEED experiment, the quantitative characterization of the stripe pattern is done by analyzing the spot profiles and studying their evolution as a function of scattering conditions. The scattering phase S is commonly used to describe the scattering conditions. The scattering phase

$$S = (K_{\perp} d) / (2\pi) = (1/h) 2d \sqrt{2m_e E} \cos \alpha$$

is varied by changing the electron energy E . Here, d is the height of a monatomic step (in the case of Cu(100): 1.8 Å), K_{\perp} denotes the vertical component of the scattering vector, h is Planck's constant, m_e the electron mass and α the angle of incidence of the electron beam. Integer values of the scattering phase indicate an in-phase condition; if the scattering phase has an half-integer value, scattering from adjacent terraces is out-of-phase.

6.2 Characterization of stripe pattern

The occurrence of the stripe pattern on the copper films could be linked to characteristic changes in the shape of the LEED spots. The exact shape of the (00) spot for a 12 ML copper film on Ni(100) as seen by a two dimensional high resolution scan is shown in Figure 6.1. One can clearly see the satellites of the LEED spot oriented along $\langle 110 \rangle$. Since the satellites are very close to the (00) spot, the cross like spot shape is obtained. The satellites of the LEED spot are caused by the pattern of stripes running along $\langle 110 \rangle$ (see Fig. 5.3).

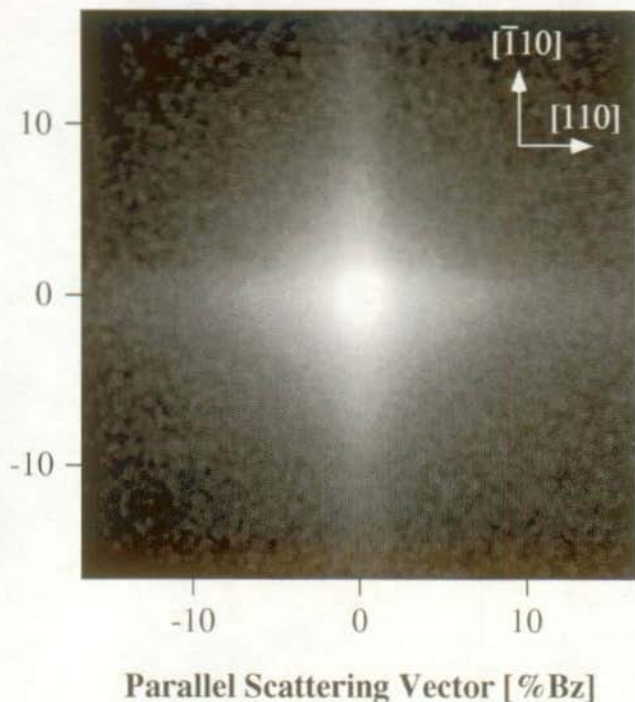


Fig. 6.1. High resolution LEED image of the specular (00) beam taken from a 11.5 ML copper film on Ni(100) grown at 350 K (deposition rate: 5×10^{-3} ML/s, electron energy: 43 eV, incidence angle: 7°). Note, the characteristic cross like shape of the spot with wings in $\langle 011 \rangle$ directions.

By means of SPA-LEED, we have been able to detect these satellites at coverages between 3 and 18 ML (substrate temperature 300 K and 350 K). With STM, we had discovered stripes at coverages as low as ~ 0.2 ML. These two observations are not in disagreement, since the fraction of the surface covered by stripes ϑ_s has to reach about 10 % to be detectable by LEED. The satellites become more and more pronounced as the film thickness increases and are best visible in the LEED

pattern between 9 and 14 ML. At still higher coverages, the LEED-spots start to ‘blur out’, until, at film thicknesses beyond 20 ML, only broad, isotropic spots occur, consistent with STM-measurements: At a coverage of 25 ML no stripes are visible and a dislocation network has formed (see Fig. 5.10).

Spot profiles have been recorded parallel to $\langle 110 \rangle$ for diffraction patterns obtained at coverages of 9.0 and 11.5 ML, where the satellites are well pronounced. Figure 6.2 shows a typical spot profile. In addition to a constant background, one can distinguish between the following contributions:

- a central peak. Its full width at half maximum (FWHM) is given by the instrument and the mosaic broadening of the sample.
- satellites in the $\langle 110 \rangle$ directions. Their position does not change with scattering conditions.
- a broad shoulder due to inhomogeneities

All parts of the spot profile were fitted using Lorentzian like profiles $\kappa^2/(\kappa^2 + \mathbf{K}_{\parallel}^2)^{3/2}$ with the help of a numerical least square fitting algorithm. This method allows to determine unambiguously the intensity and the shape of the different contributions, even though – especially at higher scattering phases – the different contributions to the spot profile tended to ‘blur out’ due to the mosaic spread of the sample and discrimination seemed to be poor.

The peak intensities vary considerably with the scattering phase due to dynamic multiple scattering effects, but the FWHM and the positions \mathbf{K}_i and \mathbf{K}_o of the satellites do not depend on electron energy. The position of the inner satellite \mathbf{K}_i gives the mean distance ℓ between stripes: $\ell = 2\pi/|\mathbf{K}_i|$. We attributed the position of the outer satellite, \mathbf{K}_o , to the width of the stripes D . The mean distance ℓ between stripes, which is independent of coverage and substrate temperature, determines the stripe density $\rho = \ell^{-2} = (7.3 \pm 1.5) \times 10^{-4}$ stripes per atom. This agrees nicely with the value found by STM: $\rho = (8.0 \pm 1.4) \times 10^{-4}$ stripes per atom.

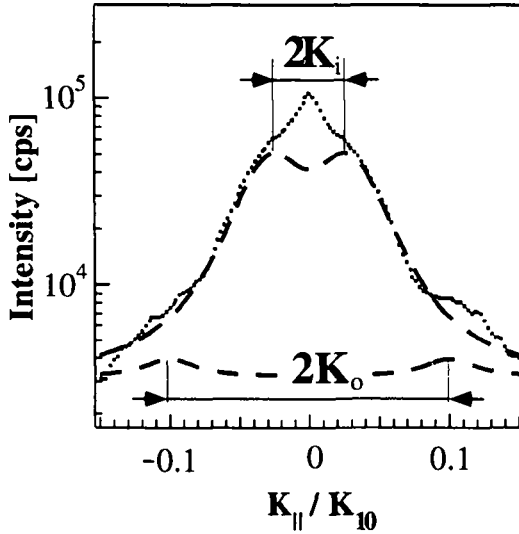


Fig. 6.2. LEED spot profile analysis of a 11.5 ML copper film on Ni(100) ($T_S=300$ K, $R=5\times 10^{-3}$ ML/s). The profile of the (00) beam at $S=1.97$ along $\langle 110 \rangle$ is displayed. For better clarity, the broad peak is subtracted from the experimental data (dots). Two pairs of satellites are clearly visible in the spot profile. The inner satellite pair is associated with the stripe separation, the outer with the stripe width.

The outer satellite is clearly visible in the experiments performed at the coverage of 11.5 ML. Its associated real space length, $D=(25\pm 5)$ Å = 10 ± 2 atoms, corresponds well with the width of the stripes. The internal faceting model gives an average stripe width of 11.5 atoms, in agreement with STM-measurements ($D = 12\pm 2$ atoms). The FWHM of the outer satellite is relatively small, indicating that there is only little variation of the stripe width as expected from the internal faceting model and the STM measurements.

In order to perform a quantitative spot profile analysis one has to use the kinematic approximation taking into account only scaled intensities to get rid of dynamic effects [Hen84]. By appropriate fitting procedures, the integral intensity of the central peak and the diffuse part, I_0 and I_d ,

are separated. At a substrate temperature of 350 K, both, the STM and the time dependent SPA-LEED measurements have shown that multi-layer films basically grow in step flow, as will be discussed in detail in the following chapter. Thus, the protruding stripes are the only relevant defect structures of the film and the effects on scattering from the few islands left at the surface can be neglected. Based on the kinematic theory for a two level system [LC84], for such a stripe pattern the scaled integral intensity of the diffuse part can be written by:

$$\frac{I_d}{I_d + I_0} = 2\vartheta_s (1 - \vartheta_s) \left[1 - \cos \left(2\pi \frac{\Delta h}{d} S \right) \right] \quad (6.1)$$

The equation describes the variation of the scaled intensity $I_d/(I_d + I_0)$ with the scattering phase S within the kinematic approximation. The scattering phase S , which is varied by changing the electron energy, is related to the height of a monatomic step. Since we consider the height of the stripes Δh , the factor $\frac{\Delta h}{d}$ has to be introduced. For the quantitative analysis of the stripe height Δh and the fraction of the surface covered by stripes ϑ_s , equation (6.1) is used. I_d is given by the integral intensity of the inner satellite and I_0 corresponds to the integral intensity of the central peak. Figure 6.3 shows two examples for the evaluation of the integral intensity as function of the scattering phase. All measured curves show a maximum close to $S = 2$, so that the ratio $\frac{\Delta h}{d}$ equals to 1/4. A more precise value is obtained by fitting the experimental data to equation (6.1). The two fitting parameters, $\frac{\Delta h}{d}$ and ϑ_s , correspond to 0.235 ± 0.010 and 0.32 ± 0.03 , respectively. Using the step height $d = \frac{1}{2} \cdot 3.61 \text{ \AA}$, the height of stripes Δh is found to be $0.42 \pm 0.02 \text{ \AA}$. By the use of $D = 10 \pm 2$ atoms, $\rho = (7.3 \pm 1.5) \times 10^{-4}$ per atom and $\vartheta_s = 0.32 \pm 0.03$, one finds the mean length of the stripes $\bar{s} = (35.5 \pm 15.0)$ atoms.

The results of the G(S)-analysis are in perfect agreement with the internal faceting model as well as with the STM-measurements. The simple hard sphere model predicts a stripe height of 0.40 \AA , a value which is also obtained by G(S) analysis ($\Delta h = 0.42 \pm 0.02 \text{ \AA}$). Even the STM gives a reasonable value ($\Delta h = 0.6 \pm 0.1 \text{ \AA}$). This cannot be necessarily expected, since height measurements by STM are not only determined by geometrical factors but also by electronic contributions [MH94, RSBK93].

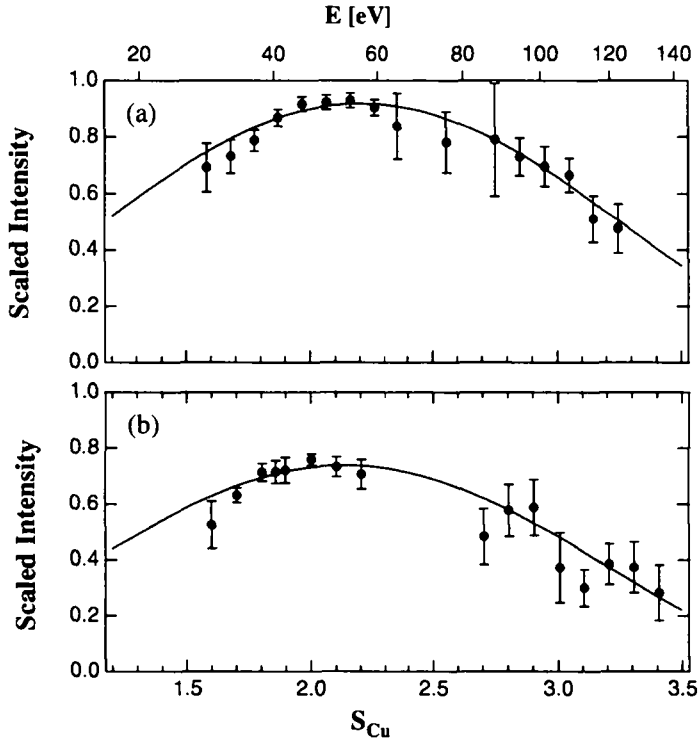


Fig. 6.3. LEED spot profile analysis (G(S)-analysis) of a 11.5 ML copper film on Ni(100) for substrate temperatures of 300 and 350 K ($R=5 \times 10^{-3}$ ML/s). Circles indicate the scaled intensity of the inner satellite, for both fits (full line), the stripe height was fixed at $\Delta h = 0.42$ Å.

6.3 Mosaic formation and characterization of the dislocation network

Above 20 ML, the network of stripes vanishes and a dislocation network was observed by STM (see Fig. 5.10, Chap. 5). The surface resembles a patchwork of tilted microterraces. Quantitatively, this tilt can be described by the mosaic spread. The standard variation of the angular distribution of mosaic spread is denoted, here, as mosaic angle φ_θ . In diffraction, the mosaic spread causes a broadening of the Bragg rods

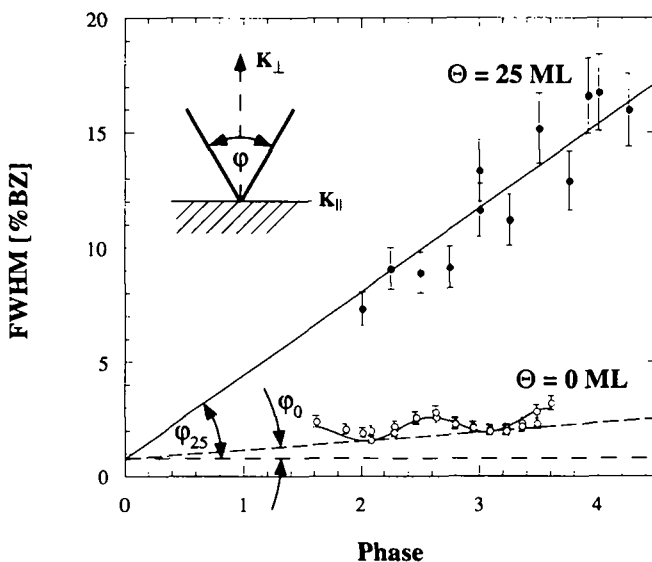


Fig. 6.4. Determination of the mosaic spread for a 25 ML copper film on Ni(100). For the substrate, a superposition of linear increase of the FWHM due to the mosaic spread $\varphi_0 = 0.16^\circ$ (dashed line) and oscillations due to atomic steps are detected. The formation of dislocations for a 25 ML film yields a dramatic increase of the mosaic spread $\varphi = 1.32^\circ$ (solid line).

into cone-shaped bunches. That means, the FWHM of the spot profiles increases with the scattering phase S [Hen84]:

$$\text{FWHM}(\theta) = \frac{a}{d} \tan \varphi_\theta S \quad (6.2)$$

where a and d are the lateral lattice constant and the interlayer distance, respectively. For fcc(100) surfaces, one finds $a/d = \sqrt{2}$.

The plot of FWHM versus S at a coverage of 25 ML is displayed in Figure 6.4 and compared to results obtained on the clean nickel substrate. For the 25 ML film, the total mosaic angle corresponds to $\varphi_{25} = 1.48^\circ \pm 0.05^\circ$. In the case of the clean sample, the linear increase of the FWHM is superimposed by oscillations due to the finite terrace length. A more complete analysis is needed to fully describe the behaviour of such a curve, it yields an average terrace length Γ of 158 ± 15 Å. For details, see p.e. Ref. [LHK⁺94]. One has to subtract the mosaic angle of the substrate ($\varphi_0 = 0.16^\circ \pm 0.02^\circ$). By subtracting the mosaic angle of the clean substrate φ_0 from the total mosaic angle φ_{25} , one obtains the mosaic angle φ inherent to the copper film. This mosaic spread of $1.32^\circ \pm 0.07^\circ$ is caused by the dislocations. Supposing a monatomic height for each dislocation, one obtains a dislocation density ρ_D of $(10.6 \pm 1.0) \times 10^{-4}$ per atom.

This value is comparable to the density of stripes ρ which is found at intermediate coverages ($\theta = 1$ –17 ML). This numerical identity strongly suggests that for thicker copper films on Ni(100), the birth of strain relieving dislocations is directly related to colliding stripes.

6.4 Limits of strain relief by internal faceting

The evolution of spot profiles during growth is reported in Figure 6.5, the results of the quantitative spot profile analysis are shown in Figure 6.6. The spot profiles were fitted numerically, and we can describe them as a superposition of a central peak and two satellites. In the fitting procedure, the FWHM of the central peak was chosen to be constant. The FWHM of the satellites does not change markedly with the coverage (see Fig. 6.6 (b)). Since the scattering phase is rather low ($S=1.55$), the sensitivity for mosaic broadening is relatively weak in this experiment. At a higher scattering phase, one finds a broadening of the FWHM with

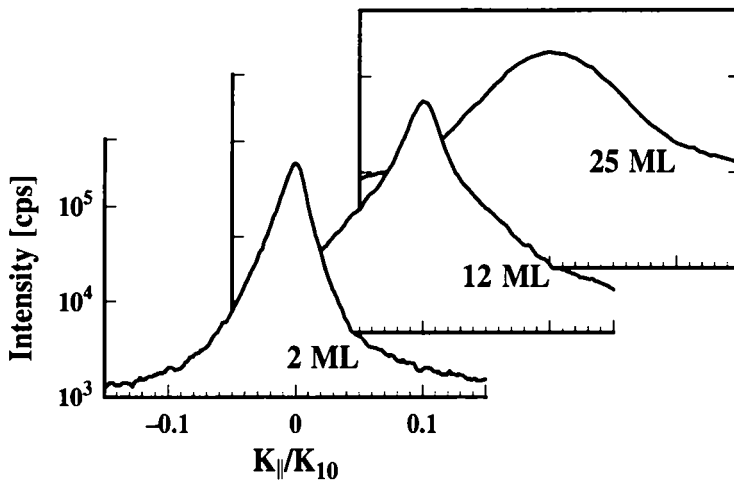


Fig. 6.5. Evolution of the LEED spot profiles during growth. Due to the stripes satellites appear at low coverage while the whole spot is dramatically broadened for thick films containing dislocations.

increasing coverage. For coverages up to 17 ML the satellites seem to move towards the central peak with coverage. However, as this tendency is weak and within the limit of experimental error, no definite conclusions can be drawn. Concerning the scaled intensity of the central peak $I_0/(I_0 + I_d)$, one expects a decrease with coverage θ according to a square law:

$$G_0(\theta) = \frac{I_0}{I_0 + I_d} = 1 - 2\vartheta_s(1 - \vartheta_s) \cos(2\pi\Delta h/d) \quad (6.3)$$

This expression is equivalent to equation (6.1), but here the integral intensity of the central peak instead of the diffusive part is considered. ϑ_s is given by the film thickness θ , $\vartheta_s = \vartheta_1 \cdot \theta$, where ϑ_1 is one of the parameters to be fitted. The minimum of the parabola given by equation (6.3) indicates that the surface is half covered by stripes (ϑ_s

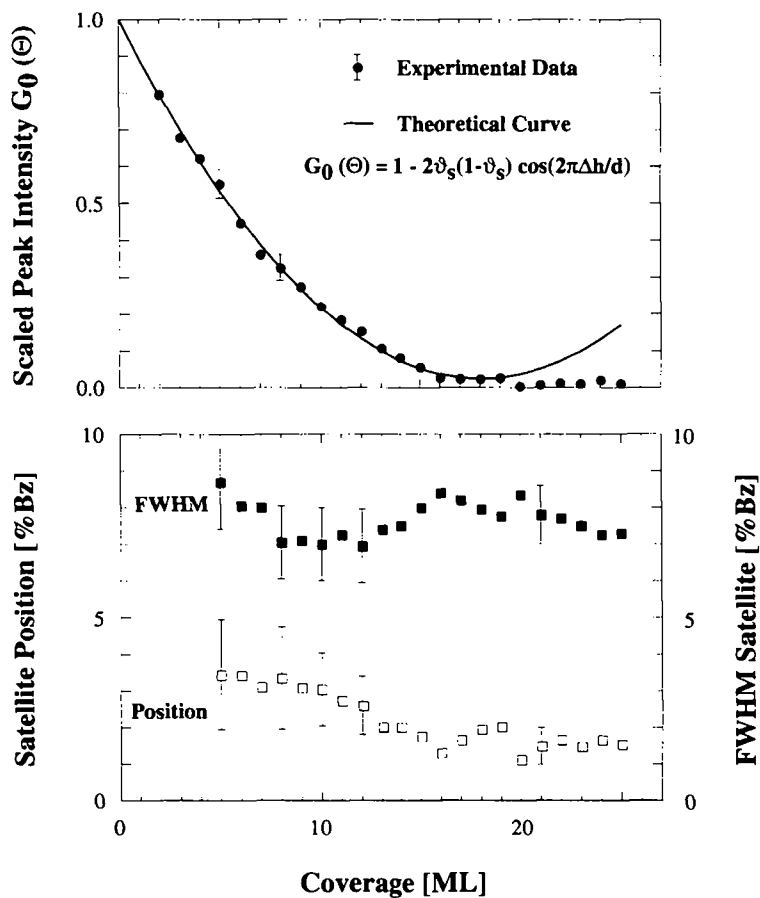


Fig. 6.6. (a) Quantitative description of peak intensity of the central LEED peak versus coverage. From the minimum of the parabola one obtains that half of the copper film is covered by stripes at (18 ± 1) ML. (b) Evolution of the satellite FWHM and the position with coverage.

= 0.5). Indeed, the experimental data fulfill such a law, the minimum corresponds to $\theta=(18\pm1)$ ML. This value is in good agreement with the spot profile analysis. Extrapolating the stripe coverage obtained from the G(S) analysis for 11.5 ML one expects a stripe coverage of 50 % at a film thickness of (18 ± 3) ML assuming the linear increase of the stripe coverage with copper coverage. STM predicts a value of (16.5 ± 2.0) ML (see Fig. 5.7(c)).

At coverage greater than 18 ML ($\vartheta_s > 0.5$) the central peak intensity does not increase again as expected from equation (6.3), but stays more or less constant. Apparently, the strain relief mechanism via internal faceting is not efficient for coverages above 18 ML. This is also supported by the disappearance of the crosslike shape of the LEED spots at this coverage. hence, the quantity introduced in section 5.6, the upper limit for an effective strain relief by internal faceting, was found to be $h^* = 18 \pm 1$ ML. From 18 ML onwards, strain is no longer relieved via internal facets, but by the formation of dislocations. This leads to surface structures as shown in Figure 5.10 and described quantitatively in Figure 6.4.

It should be mentioned that Cu/Ni(100) can indeed be described as a two level system, an assumption upon which the spot profile analysis according to equation (6.1) is based. The LEED measurements during growth reveal that this assumption is fulfilled at a substrate temperature of 345 K, since the decrease in peak intensity is fully explained by the growth of the stripe pattern as given by equation (6.3).

6.5 Conclusion

The diffraction technique SPA-LEED allowed us to characterize with high precision the stripe network caused by the internal faceting. This is especially important concerning the stripe height Δh , since STM images are an account on the topological *and* the electronic structure of the surface.

The value obtained by STM ($\sim 1/3$ step height) does not deviate drastically from the results of the SPA-LEED measurements ($\sim 1/4$ step

height). However, the precise determination of the step height offers hints concerning some details of the internal structure of the stripes (see Section 5.4).

Chapter 7

Growth kinetics in the multilayer range

7.1 Nucleation and surface roughness at multilayer coverage

The STM measurements have shown that copper on Ni(100) grows at 345 K in the first two monolayers in a layer-by-layer fashion and above a coverage of 2 ML even in the step flow mode. With the SPA-LEED, we monitored the intensity of the (00) spot during growth at out-of-phase condition; Figure 7.1 shows a typical example. The characteristic curves can be easily explained by comparison with the STM results:

Intensity oscillations are present during the growth of the first two monolayers. Note, the intensity minimum at $\theta=0.5$ ML is pronounced and the first maximum at $\theta=1$ ML weak. This is consistent with the STM results which show the highest saturation island density in the first layer and the onset of nucleation in the second layer starting before the first layer is completed (see Fig. 5.2 and Fig. 5.3(a)). At coverage above 2 ML no oscillations occur, the intensity decreases monotonously. This means, for coverage $\theta > 2$ ML, we do not observe island formation within the transfer width of the SPA-LEED instrument. Usually one expects constant peak intensity for the step flow mode. Here, however,

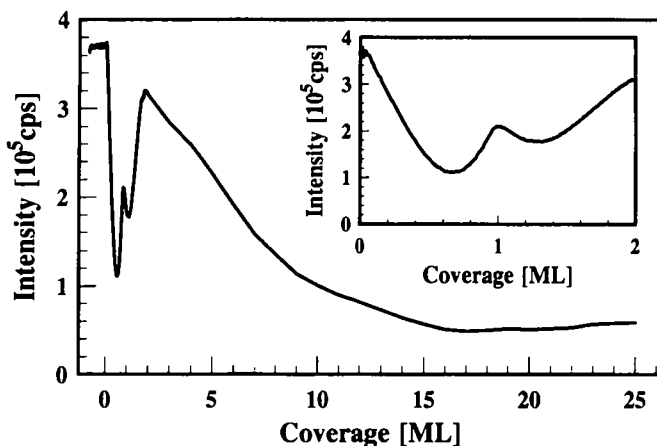


Fig. 7.1. Evolution of the peak intensity of the (00) LEED spot during epitaxial growth of copper on Ni(100). ($T_s=350$ K, $R=5\times 10^{-3}$ ML/s, $S=1.55$). The first two layers oscillations are related to 2D-islands. Above 2 ML, the film grows in the step flow mode and the attenuation of the peak intensity is only caused by the increasing stripe coverage.

the intensity is attenuated by the destructive interference between the elevated stripes and the terraces.

This observation confirms the STM measurements (see Fig. 5.3): Island densities in the first and in the second layer are elevated and correspond to a mean islands separation of 100–150 Å. At higher coverage we found only few islands on large terraces, with an island separation greater than 600 Å. Because the average terrace width is smaller, the film grows in step flow and one detects only flat terraces.

The increased island density in the first copper layers is of kinetic origin. While at the submonolayer level the nucleation kinetics is determined by the copper–nickel interaction, with increasing film thickness the film adopts more and more a copper like behaviour, i.e. finally the nucleation kinetics will resemble those of Cu/Cu(100).

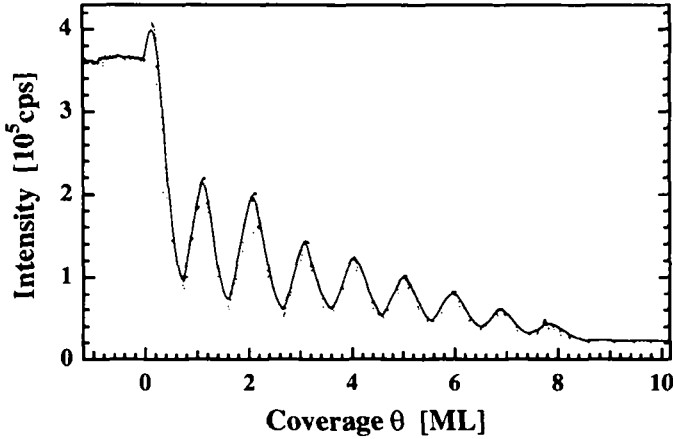


Fig. 7.2. Evolution of the peak intensity of the (00) LEED spot during epitaxial growth of copper on Ni(100) at low temperature ($T_s=125$ K, $R=5\times 10^{-3}$ ML/s, $S=1.55$). The initial increase of specular intensity at $\theta = 0$ –0.2 ML may be related to the different form factors of copper and nickel. The deposition had been interrupted at a coverage of $\theta = 8.5$ ML.

For copper on Ni(100), the migration barrier E_m , the dimer bond energy E_b and the size of the critical nucleus have been determined in Chapter 3. Concerning the same quantities for the homoepitaxial system copper on Cu(100), differing results have been reported (see Table 3.1). For the reasons discussed in Section 3.2.3, we will rely on the values given by Bartelt and Evans [EB96].

For migration of copper and nickel on Ni(100), the migration barriers are equal within the error bars, (0.35 ± 0.02) eV (Ni(100)) and ~ 0.36 eV (Cu(100)) [EB96], while the dimer bond energies differ by a factor of approximately 2.5¹ (0.46 ± 0.19) eV (Ni(100)) vs. 0.20 eV (Cu(100)) [EB96].

¹The results of Dürr *et al.* suggest even a factor of ~ 5 with $E_b = 0.06$ [ZWDL94, DWZ95]. We consider this binding energy to be too low; however, such a small binding energy would result in an even lower island density and thus accentuate the observed step flow mode.

The tetramer is the smallest stable island at room temperature in both cases. In this case, the saturation island density n_s is described correctly by equation (3.13) if one sets the size of the critical nucleus $i = 3$. As the migration barriers for copper on Cu(100) and copper on Ni(100) are nearly identical, the substantial difference in the dimer bond energy is the physical reason for the coverage dependent island density. Indeed, assuming a critical island size of 3 and $E_m = 0.35$ eV, a difference of the bond energy by 0.26 eV results in a difference in the island densities by a factor of ~ 30 , in good agreement with the experimental observation.

Figure 7.2 shows intensity oscillations of the (00) during deposition at low temperatures $T_s = 125 \pm 7$ K. At these temperatures, copper on Ni(100) as well as copper on Ni(100) show a reduced adatom mobility. In both cases, the size of the critical nucleus is one. Hence, the differing binding energies do not intervene in the growth scenario, and, concerning the number of nucleation sites and surface roughness, there is no principal difference between the building up of the first, the second or a later layer. Indeed, one observes well pronounced intensity oscillations until high coverage. However, these oscillations are enveloped by a pronounced decay, indicating a substantial raise in surface roughness. This increased surface roughness should at least partially be caused by the formation of the strain relieving stripes.

Chapter 8

Conclusion

The epitaxial growth of copper on nickel(100) has been extensively studied. This system is a model system for heteroepitaxial growth under weak compressive strain. The positive misfit influences the thin film morphology in almost all stages of the growth, even at submonolayer coverage.

In the submonolayer range, the misfit causes larger copper islands to become ramified independent on the growth conditions. For intermediate coverage ($\theta = 0.2$ – 17 ML), a novel strain relief mechanism has been uncovered: internal $\{111\}$ faceting. Films thicker than 18 monolayers show a mosaic spread due to accumulated strain which is related to the formation of a dislocation network.

Only at very low coverages, i.e. for island sizes ≤ 500 atoms, misfit related effects are weak. The systematic variation of the growth parameters – substrate temperature and deposition flux – and the application of the mean field nucleation theory are used to extract the microscopic parameters: the activation barrier of adatom terrace migration, the dimer bond energy, the related attempt frequency and the sizes i of the critical nuclei. The square symmetry of the substrate is responsible for a direct transition from $i = 1$ to $i = 3$. These microscopic parameters are necessary to simulate the growth, e.g. by using rate equations. Rate equations are applied to the $i = 1$ regime, and at lower temperature post-deposition is studied in detail.

Scanning tunneling microscopy (STM) and spot profile analysis of low energy electron diffraction (SPA-LEED) are complementary methods in Surface Physics, and the study of the Cu/Ni(100) system allowed us to compare the pros and cons of both methods.

STM is a local probe method giving unprecedented microscopic insights in growth phenomena. Reciprocal space methods can also give access to atomistic growth processes, their application bears, however, certain disadvantages. For example, in the study of nucleation phenomena (comp. Chapter 3), with STM it is straightforward to obtain a real space view of nucleation, count the island density, measure the island size distribution or determine the average island separation. Diffraction techniques, on the other hand, have difficulties to characterize islands at small coverage (<0.1 ML). In addition, they require a certain preknowledge about island size and separation distributions in order to extract distances and densities in real space. Opposite to local probe methods, the averaging character of reciprocal space techniques yields a high statistical significance, at the same time it can be a disadvantage since areas with defects such as substrate steps are included in the average.

The situation is inverse concerning the structural analysis of epitaxial films. STM quite often provides a qualitative picture but the quantitative analysis is difficult. An example is the determination of step heights. STM has difficulties due to electronic contributions which can distort the determination of surface morphology. With diffraction techniques, on the other hand, the determination of height differences is straightforward (comp. Chapter 6). Only, at complex surfaces the interpretation of diffraction experiments is not necessarily singlevalued and demands a careful analysis. The qualitative picture provided by STM can offer a valuable starting point. In any case the major advantage of integrating reciprocal space techniques is their high statistical significance which yields numerical results with high precision. In addition diffraction techniques can provide data which are often not accessible by the local probe methods such as STM. For example, the evaluation of mosaic angles is straightforward with SPA-LEED (see Section 6.3).

In addition, SPA-LEED is better suited for *in situ* studies during deposition (see Section 3.2.5).

Local real space microscopy and integrating reciprocal space diffraction experiments are largely complementary techniques. The synergism

between both experimental approaches allowed us a detailed characterization of the epitaxial growth phenomena occurring for copper growth on nickel(100).

Bibliography

- [AF95] J. G. Amar and F. Family, *Critical cluster size: Island morphology and size distribution in submonolayer epitaxial growth*, Phys. Rev. Lett. **74** (1995), 2066.
- [Bal70] C. A. B. Ball, *On bonding and structure of epitaxial bicrystals*, Phys. Stat. Sol. **42** (1970), 357.
- [Bau58] E. Bauer, *Phänomenologische Theorie der Kristallabscheidung an Oberflächen*, Z. Kristallogr. **110** (1958), 372.
- [BB92] M. Breeman and D. O. Boerma, *Migration of Cu adatoms on a Cu(100) surface, studied with low energy ion scattering*, Surf. Sci. **269/270** (1992), 224.
- [BBEB90] J. V. Barth, H. Brune, G. Ertl, and R. J. Behm, *Scanning tunneling microscopy observations on the reconstructed Au(111) surface: Atomic structure, long-range superstructure, rotational domains and surface defects*, Phys. Rev. B **42** (1990), 42.
- [BBK⁺96] H. Brune, K. Bromann, K. Kern, J. Jacobsen, P. Stoltze, K. Jacobsen, and J. Nørskov, *Fractal and dendritic growth of surface aggregates*, Mat. Res. Soc. Symp. Proc. **407** (1996), 379.
- [BC94] G. S. Bales and G. D. Chrzan, *Dynamics of irreversible island growth during submonolayers epitaxy*, Phys. Rev. B **50** (1994), 6057.
- [BE92] M. C. Bartelt and J. W. Evans, *Scaling analysis of diffusion-mediated island growth in surface adsorption processes*, Phys. Rev. B **46** (1992), 12675.
- [Bes] *Besocke-delta-phi-elektronik*, Postfach 2243, 52428 Jülich, FRG.
- [Bes87] K. Besocke, *An easily operable scanning tunneling microscope*, Surface Science **181** (1987), 145.
- [BF95] J. V. Barth and D. E. Fowler, *Low-coverage nonpseudomorphic and metastable structures of magnetic Fe on Cu(001)*, Phys. Rev. B **52** (1995), 11432.

- [BHF⁺94] J.-P. Bucher, E. Hahn, P. Fernandez, C. Massobrio, and K. Kern, *Transition from one- to two-dimensional growth of Cu on Pd(110) promoted by cross-exchange migration*, Europhys. Lett. **27** (1994), 473.
- [BHM⁺96] M. Bott, M. Hohage, M. Morgenstern, T. Michely, and G. Comsa, *New approach for determination of diffusion parameters of adatoms*, Phys. Rev. Lett. **76** (1996), 1304.
- [BK96] H. Brune and K. Kern, *Heteroepitaxial metal growth: the effects of strain*, in The Physics and Chemistry of Solid Surfaces (King and Woodruff, eds.), vol. 8, 1997, in press.
- [BMC92] M. Bott, T. Michely, and G. Comsa, *The homoepitaxial growth of Pt on Pt(111) studied with STM*, Surf. Sci. **272** (1992), 161.
- [BPE95] M. C. Bartelt, L. S. Perkins, and J. W. Evans, *Transitions in critical size for metal (100) homoepitaxy*, Surf. Sci. **344** (1995), L1193.
- [BR82] G. Binnig and H. Rohrer, *Scanning tunneling microscopy*, Helv. Phys. Acta **55** (1982), 726.
- [BRB⁺96] H. Brune, H. Röder, K. Bromann, K. Kern, J. Jacobsen, P. Stoltze, K. Jacobsen, and J. Nørskov, *Anisotropic corner diffusion as origin for dendritic growth on hexagonal substrates*, Surf. Sci. **349** (1996), L115.
- [BRBK94a] H. Brune, H. Röder, C. Boragno, and K. Kern, *Microscopic view of nucleation on surfaces*, Phys. Rev. Lett. **73** (1994), 1935.
- [BRBK94b] H. Brune, H. Röder, C. Boragno, and K. Kern, *Strain relief at hexagonal close-packed-interfaces*, Phys. Rev. B **49** (1994), 2997.
- [BRBK95] H. Brune, H. Röder, K. Bromann, and K. Kern, *Kinetic processes in metal epitaxy studied with variable temperature STM: Ag/Pt(111)*, Thin Solid Films **264** (1995), 230.
- [BRGW82] G. Binnig, H. Rohrer, C. Gerber, and E. Weibel, *Surface studies by scanning tunneling microscopy*, Phys. Rev. Lett. **49** (1982), 57.
- [BRRK94] H. Brune, C. Romanezyk, H. Röder, and K. Kern, *Mechanism of the transition from fractal to dendritic growth of surface aggregates*, Nature **369** (1994), 469.
- [BS86] G. Binnig and D. P. E. Smith, *Single-tube three dimensional scanner for scanning tunneling microscope*, Rev. Sci. Instrum. **57** (1986), 1688.
- [BSS⁺95] M. Brandbyge, J. Schiøtz, M. R. Sørensen, P. Stoltze, K. W. Jacobsen, and J. K. Nørskov, *Quantized conductance in atomic-sized wires between two metals*, Phys. Rev. B **52** (1995), 8499.
- [BZ86] R. Bruinsma and A. Zangwill, *Structural transitions in epitaxial overlayers*, J. Phys. (Paris) **47** (1986), 2055.

- [CC92] D. D. Chambliss and S. Chiang, *Surface alloy formation studied by scanning tunneling microscopy: Cu(100) + Au-c(2x2)*, Surf. Sci. Lett. **264** (1992), L187.
- [CCV+86a] S. A. Chambers, H. W. Chen, I. M. Vitomirov, S. B. Anderson, and J. H. Weaver, *Direct observation of elastic strain and relaxation at a metal-metal interface by auger electron diffraction: Cu/Ni(001)*, Phys. Rev. B **33** (1986), 8810.
- [CCV+86b] S. A. Chambers, H. W. Chen, I. M. Vitomirov, S. B. Anderson, and J. H. Weaver, *Direct observation of elastic strain and relaxation at a metal-metal interface by auger electron diffraction: Cu/Ni(001)*, Phys. Rev. B **33** (1986), 8810.
- [CH95] C. B. Carter and R. Q. Hwang, *Dislocations and the reconstruction of (111) fcc metal surfaces*, Phys. Rev. B **51** (1995), 4730.
- [CJ75] A. Chambers and D. C. Jackson, *The growth and structure of thin copper films on (001) surfaces of nickel*, Philos. Mag. **31** (1975), 1357.
- [CJ94] D. D. Chambliss and K. E. Johnson, *Nucleation with a critical cluster size of zero: Submonolayer Fe inclusions in Cu(100)*, Phys. Rev. B **50** (1994), 5012.
- [DKZC86] R. David, K. Kern, P. Zeppenfeld, and G. Comsa, *High-resolution He-scattering apparatus for gas-surface interaction studies*, Rev. Sci. Instrum. **57** (1986), 2771.
- [DSC+87] J. DeMiguel, A. Sánchez, A. Cebollada, J. M. Gallego, J. Ferrón, and S. Ferrer, *The surface morphology of a growing crystal studied by thermal energy atom scattering (TEAS)*, Surf. Science **189/190** (1987), 1062.
- [DWZ95] H. Dürr, J. F. Wendelken, and J. K. Zuo, *Island morphology and adatom energy barriers during homoepitaxy on Cu(001)*, Surf. Sci. **328** (1995), L527.
- [EB96] J. W. Evans and M. C. Bartelt, *Submonolayer island formation and subsequent multilayer kinetic roughening during metal(100) homoepitaxy: Fe, Ag & Cu*, in Surface Diffusion: Atomistic and Collective Processes (M. Scheffler and M. C. Tringides, eds.), NATO ASI, Series B: Physics, 1996, in press.
- [EFL92] H. J. Ernst, F. Fabre, and J. Lapujoulade, *Nucleation and diffusion of Cu adatoms on Cu(001): A helium-atom-beam scattering study*, Phys. Rev. B **46** (1992), 1929.
- [EJ89] W. F. Egelhoff and I. Jacob, *Reflection high-energy electron diffraction (RHEED) oscillations at 77 K*, Phys. Rev. Lett. **62** (1989), 921.

- [EK85] G. Ertl and J. Küppers, Low energy electrons and surface chemistry, VCH, Weinheim, 1985.
- [FBF⁺] B. Fischer, J. Barth, A. Fricke, L. Nedelmann, and K. Kern, *Growth and surface alloy formation of Al on Au(111)*, submitted.
- [FCS⁺94] J. Faist, F. Capasso, D. L. Sivco, C. Sirtori, A. L. Hitchinson, and A. Y. Cho, *Quantum cascade laser*, Science **264** (1994), 553.
- [FK39] J. Frenkel and T. Kontorova, *On the theory of plastic deformation and twinning*, J. Phys. (USSR) **1** (1939), 137.
- [FvdM49] F. C. Frank and J. H. van der Merwe, *One-dimensional dislocations*, Proc. Roy. Soc. London A **198** (1949), 205.
- [FWBT89] J. Frohn, J. F. Wolf, K. Besocke, and M. Teske, *Coarse tip distance adjustment and positioner for a scanning tunneling microscope*, Rev. Sci. Instrum. **60** (1989), 1200.
- [GKB⁺94] S. Günther, E. Kopatzki, M. C. Bartelt, J. W. Evans, and R. J. Behm, *Anisotropy in nucleation and growth of two-dimensional islands during homoepitaxy on 'hex' reconstructed Au(100)*, Phys. Rev. Lett. **73** (1994), 553.
- [GVHB95] C. Günther, J. Vrijmoeth, R. Q. Hwang, and R. J. Behm, *Strain relaxation in hexagonally close-packed metal-metal interfaces*, Phys. Rev. Lett. **74** (1995), 754.
- [HB92] R. Q. Hwang and R. J. Behm, *Scanning tunneling microscopy studies on the growth and structure of thin metallic films on metal substrates*, J. Vac. Sci. Technol. B **10** (1992), 256.
- [Hen84] M. Henzler, *Defects at surfaces*, in Dynamical Phenomena at Surfaces, Interfaces and Superlattices (F. Nizzoli, K. H. Rieder, and R. F. Willes, eds.), Springer Series in Surface Science, vol. 3, Springer Berlin, 1984.
- [HG94] M. Henzler and W. Göpel, Oberflächenphysik des Festkörpers, Second ed., Teubner, Stuttgart, 1994.
- [HHMW95] M. Henzler, C. Homann, U. Malaske, and J. Wollschläger, *Misfit accommodation in heteroepitaxy by inclined stacking faults*, Phys. Rev. B **52** (1995), 17060.
- [HHS96] B. Herzog, D. Herein, and R. Schlögl, *In-situ x-ray-powder diffraction analysis of the microstructure of activated iron catalysts for ammonia-synthesis*, Applied Catalysis A **141** (1996), 71.
- [HKWK95] E. Hahn, E. Kampshoff, N. Wälchli, and K. Kern, *Strain driven fcc-bcc phase transition of pseudomorphic Cu films on Pd(100)*, Phys. Rev. Lett. **74** (1995), 1803.

- [HSGB91] R. Q. Hwang, J. Schröder, C. Günther, and R. J. Behm, *Fractal growth of two-dimensional islands: Au on Ru(0001)*, Phys. Rev. Lett. **67** (1991), 3279.
- [Iba86] H. Ibach, *Herstellung und Charakterisierung reiner Oberflächen*, in Dünne Schichten und Schichtsysteme, 17. IFF Ferienkurs, Kernforschungsanlage Jülich, 1986.
- [Jac88] K. W. Jacobsen, *Bonding in metallic systems: An effective-medium approach*, Comments Cond. Mat. Phys. **14** (1988), 129.
- [JCP] JCPDS-ICDD database.
- [JKP+92] O. Jusko, U. Köhler, G. Pietsch, B. Müller, and M. Henzler, *Trench formation in surfactant mediated epitaxial film growth of Ge on Si(100)*, Appl. Phys. A **54** (1992), 265.
- [JKW67] W. A. Jesser and D. Kuhlmann-Wilsdorf, *On the theory of interfacial energy and elastic strain of epitaxial overgrowths in parallel alignment on single crystal substrates*, Phys. Stat. Sol. **19** (1967), 95.
- [Kel94] G. L. Kellogg, *Field ion microscopy studies of single-atom surface diffusion and cluster nucleation on metal surfaces*, Surf. Sci. Rep. **21** (1994), 1.
- [KGNPB93] E. Kopatzki, S. Günther, W. Nichtl-Pecher, and R. J. Behm, *Homoeptitaxial growth on Ni(100) and its modification by a preadsorbed oxygen adlayer*, Surf. Sci. **284** (1993), 154.
- [LA92] C. Liu and J. B. Adams, *Diffusion mechanisms on Ni surfaces*, Surf. Sci. **265** (1992), 262.
- [LC84] C. S. Lent and P. I. Cohen, *Diffraction from stepped surfaces*, Surf. Sci. **139** (1984), 121.
- [LCT89] F. K. LeGoues, M. Copel, and R. Tromp, *Novel strain-induced defects in thin molecular-beam-epitaxial layers*, Phys. Rev. Lett. **63** (1989), 1826.
- [LHK+94] E. Z. Luo, S. Henn, M. Kennedy, J. Wollschläger, and M. Henzler, *Surface roughness and conductivity of thin Ag films*, Phys. Rev. B **49** (1994), 4858.
- [Lid95] D. R. Lide (ed.), Handbook of chemistry and physics, 76. ed., CRC Press (Boca Raton – New York – London – Tokyo), 1995.
- [Lin91] H. Lindner, *Wechselwirkung von Sauerstoff und Kohlendioxid mit Nickeloberflächen*, Dissertation, Universität Erlangen-Nürnberg, 1991.
- [Liu94] C. L. Liu, *Energetics of diffusion processes during nucleation and growth for the Cu/Cu(100) system*, Surf. Sci. **316** (1994), 294.

- [LMJ+96] T. R. Linderoth, J. J. Mortensen, K. W. Jacobsen, E. Laegsgaard, I. Stensgaard, and F. Besenbacher, *Homoepitaxial growth of Pt on Pt(001)-hex: Effects of strongly anisotropic diffusion and finite island sizes*, Phys. Rev. Lett. **77** (1996), 87.
- [Mar96] I. Markov, *Surface energetics from analysis of nucleation data in metal homoepitaxy*, in Surface Diffusion: Atomistic and Collective Processes (M. Scheffler and M. C. Tringides, eds.), NATO ASI, Series B: Physics, 1996, in press.
- [Mat75] J. W. Matthews (ed.), Epitaxial growth, Academic Press, New York - San Francisco - London, 1975.
- [MB95] J. A. Meyer and R. J. Behm, *Place exchange mechanism for adlayer island nucleation during epitaxial growth and resulting scaling behavior*, Surf. Sci. **322** (1995), 1,275.
- [MBT88] T. Michely, K. H. Besocke, and M. Teske, *A combined scanning tunneling and field ion microscope*, J. Microscopy **152** (1988), 77.
- [MC70] J. W. Matthews and J. L. Crawford, *Accommodation of misfit between single-crystal films of nickel and copper*, Thin Solid Films **5** (1970), 178.
- [Mea88] P. Meakin, *The growth of fractal aggregates and their fractal measures*, in Phase Transitions and Critical Phenomena (C. Domb and J. L. Lebowitz, eds.), vol. 12, Academic Press, 1988, p. 335.
- [MH94] Y. W. Mo and F. J. Himpsel, Phys. Rev. B **50** (1994), 7868.
- [MHBC93] T. Michely, M. Hohage, M. Bott, and G. Comsa, *Inversion of growth speed anisotropy in two dimensions*, Phys. Rev. Lett. **70** (1993), 3943.
- [MNF⁺] B. Müller, L. Nedelmann, B. Fischer, H. Brune, and K. Kern, *Initial stages of Cu epitaxy on Ni(100): Post-nucleation and a well defined transition in critical island size*, Phys. Rev. B, accepted.
- [MSB95] J. A. Meyer, P. Schmid, and R. J. Behm, *Effect of layer-dependent adatom mobilities in heteroepitaxial metal film growth: Ni/Ru(0001)*, Phys. Rev. Lett. **74** (1995), 3864.
- [PD94] L. S. Perkins and A. E. DePristo, *Heterogeneous adatom diffusion on fcc(100) surfaces: Ni, Cu, Rh, Pd, and Ag*, Surf. Sci. **319** (1994), 225.
- [RBBK93] H. Röder, H. Brune, J.-P. Bucher, and K. Kern, *Changing morphology of metallic monolayers via temperature controlled heteroepitaxial growth*, Surf. Sci. **298** (1993), 121.
- [Rei86] K. Reichelt, *Keimbildung und Wachstum dünner Schichten*, in Dünne Schichten und Schichtsysteme, 17. IFF Ferienkurs, Kernforschungsanlage Jülich, 1986.

- [RHB+93] H. Röder, E. Hahn, H. Brune, J.-P. Bucher, and K. Kern, *Building one- and two-dimensional nanostructures by diffusion-controlled aggregation at surfaces*, *Nature* **366** (1993), 141.
- [Röd91] H. Röder, *Aufbau und Test einer UHV-Kombinationsapparatur: Rastertunnelmikroskopie und IR-Spektroskopie an Halbleiteroberflächen*, Diplomarbeit, Rheinische Friedrich-Wilhelms-Universität Bonn, 1991.
- [Röder94] H. Röder, *Microscopic processes in heteroepitaxial growth: nucleation, growth and alloying of silver on the (111) surface of platinum*, Thèse 1288, EPF Lausanne, 1994.
- [RSBK93] H. Röder, R. Schuster, H. Brune, and K. Kern, *Monolayer confined mixing at the Ag-Pt(111) interface*, *Phys. Rev. Lett.* **71** (1993), 2086.
- [Sch95] F. Schäfer, Diplomarbeit, Universität Hannover, 1995.
- [SD79] M. P. Seah and W. A. Dench, *Quantitative electron spectroscopy of surfaces: A standard data base for electron inelastic mean free paths in solids*, *Surf. Interface Anal.* **1** (1979), 2, quoted after [HG94].
- [SG76] M. F. Sykes and M. Glen, *Percolation processes in two dimensions I. low density series expansions*, *J. Phys. A. Math. Gen.* **9** (1976), 87.
- [Sin83] J. H. Sinfelt, *Bimetallic catalysts: Discoveries, concepts and applications*, John Wiley & Sons, New York Chichester Brisbane Toronto Singapore, 1983.
- [SMH86] U. Scheithauer, G. Meyer, and M. Henzler, *A new LEED instrument for quantitative spot profile analysis*, *Surf. Sci.* **178** (1986), 441.
- [SP94] J. A. Stroscio and D. T. Pierce, *Scaling of diffusion-mediated island growth in iron-on-iron homoepitaxy*, *Phys. Rev. B* **49** (1994), 8522.
- [SPD93] J. A. Stroscio, D. T. Pierce, and R. A. Dragoset, *Homoepitaxial growth of iron and a real space view of reflection-high-energy-electron diffraction*, *Phys. Rev. Lett.* **70** (1993), 3615.
- [SSV93] M. Schmid, H. Stadler, and P. Varga, *Direct observation of surface chemical order by scanning tunneling microscopy*, *Phys. Rev. Lett.* **70** (1993), 1441.
- [Sto94] P. Stoltze, *Simulations of surface defects*, *J. Phys. Condens. Matter* **6** (1994), 9495.
- [SVK96] M. Straub, B. Vollmer, and J. Kirschner, *Phys. Rev. Lett.* **77** (1996), 743.
- [TFW92] J. Thomassen, B. Feldmann, and M. Wuttig, *Growth, structure and morphology of ultrathin iron films on Cu(100)*, *Surf. Sci.* **264** (1992), 406.

- [Ven73] J. A. Venables, *Rate equation approaches to thin film nucleation kinetics*, Philos. Mag. **17** (1973), 697.
- [VSH84] J. A. Venables, G. D. T. Spiller, and M. Hanbücken, *Nucleation and growth of thin films*, Rep. Prog. Phys. **47** (1984), 399.
- [Wal62] D. Walton, *Nucleation of vapor deposits*, J. Chem. Phys. **37** (1962), 2182.
- [Wol] J. Wollschläger, private communication.
- [WWB⁺89] J. Wintterlin, J. Wiechers, H. Brune, T. Gritsch, H. Höfer, and R. J. Behm, *Atomic-resolution imaging of close-packed metal surfaces by scanning tunneling microscopy*, Phys. Rev. Lett. **62** (1989), 59.
- [Zan93] A. Zangwill, *Scaling description of sub-monolayer epitaxial growth*, in Evolution of Surface and Thin Film Microstructure (H. A. Atwater, E. Chason, M. H. Grabow, and M. G. Lagally, eds.), vol. 280, Materials Research Society, Symposium Proceedings, 1993, p. 121.
- [ZCL94] Z. Zhang, X. Chen, and M. G. Lagally, *Bonding-geometry of fractal growth on metal surfaces*, Phys. Rev. Lett. **73** (1994), 1829.
- [Zin71] G. Zinsmeister, *Theory of thin film condensation. part D: Influence of a variable collision factor*, Thin Solid Films **7** (1971), 51.
- [ZWDL94] J. K. Zuo, J. F. Wendelken, H. Dürr, and C. L. Liu, *Growth and coalescence in submonolayer homoepitaxy on Cu(100) studied with high-resolution low-energy-electron diffraction*, Phys. Rev. Lett. **72** (1994), 3064.
- [ZWTE96] T. Zambelli, J. Wintterlin, J. Trost, and G. Ertl, *Identification of the 'active sites' of a surface catalyzed reaction*, Science **273** (1996), 1688.

Acknowledgements – Merci!

Je tiens à exprimer ma gratitude aux personnes suivantes:

d'abord à mon Directeur de thèse, le Prof. K. Kern, qui m'a donné la possibilité de faire ce doctorat en m'accueillant dans son groupe et qui a partagé les joies et les frustrations de ce travail,

à Alex Fricke, auquel je dois une bonne partie de mes connaissances de l'ultravide, du STM et des stations de ski des alentours,

à Bert Müller, qui, dès son arrivée à Lausanne, se chargea de la supervision scientifique au quotidien. Merci pour les maints tuyaux – scientifiques, rédactionnels et autres – en particulier pendant l'écriture de cette thèse.

à Bjørn Fischer, mon camarade et fidèle coéquipier, avec lequel j'ai passé de nombreuses heures en mesures, bricolage et leçons de français. Bonne chance pour la suite, Bjørn!

à Harald Brune, qui a été toujours présent en cas d'un problème, que ce soit un problème de STM ou la compréhension du *nième* coefficient de la théorie de nucleation, que ce soit ...

à MM. les membres du jury, Prof. B. Deveaud-Pledran, Dr. R. Gotthardt, Dr. C. Boragno et Dr. J. Wollschläger d'avoir bien voulu juger ce travail. A Joachim Wollschläger, je dois les excellents

souvenirs de la période de mesures 'SPA-LEED'. Son humour contagieux et l'enthousiasme de Daniel Erdős ont beaucoup contribué à rendre cette période à Hannover agréable.

à Karin Ostwald pour son hospitalité lors de mon séjour à Hannover,

à Tomaso Zambelli pour l'introduction à HIPPO,

à Alexander Bittner pour les nombreux coups de main qu'il m'a donné lors de la phase 'critique' de la rédaction de la thèse ainsi que pour son hospitalité et son amitié,

à Philippe Blandin pour son aide linguistique, la lecture critique du manuscrit et des discussions enrichissantes,

à Claire-Lise Bandelier, qui a réalisé la plupart des figures de la thèse, pour l'énorme travail qu'elle y a investi,

à "Dédé" André Guisolan, Philippe Zurcher, Philippe Cordey et tous les autres membres des ateliers mécanique et électronique pour leur soutien efficace pendant ma thèse,

à toute l'équipe de l'IPE pour la bonne ambiance et le plaisir que nous avons eu, au sein de l'institut et ailleurs,

à mes parents,

à Egle Conforto, pour son appui permanent et son affection,

à "SOS Futures Mères en Detresse" et aux "Allocations Familiales et de Maternité du Canton de Vaud" pour le support financier qu'a reçu notre petit ménage pendant ma dernière année de thèse,

au Deutsche Akademische Austauschdienst pour son soutien financier (DAAD-Doktorandenstipendium aus Mitteln des zweiten Hochschulsonderprogrammes).

Finalement, j'aimerais m'excuser auprès de Déborah, pour le temps que son père n'a pas su lui dédier pendant sa première année de vie.

Curriculum vitae

Données personnelles

nom:	Lorenz P. Nedelmann
né:	16 juillet 1966 à Buchholz/Allemagne
nationalité:	allemande
état civil:	célibataire

Formation

1972 – 1976	Scolarité obligatoire à Rödermark/Allemagne
1976 – 1985	Lycée: Adolf-Reichwein-Gymnasium, Heusenstamm/Allemagne
Okt. 1985 – Mars 1986	Stage linguistique à l'Université d'Aix-en-Provence
Avril 1986 – Nov. 1992	Etudes de chimie à la Technischen Hochschule Darmstadt. Durant cette période, deux stages ont été effectués:
1988/1989	Séjour d'une année scolaire à l'Université de Bordeaux comme boursier ERASMUS, études de chimie physique dans le cadre des échanges Darmstadt-Bordeaux
été 1991	Stage de 10 semaines au département de matériaux et d'interfaces de l'Institut Weizmann/Israël
1.4.92–2.11.92	Travail de diplôme à la Technische Hochschule Darmstadt, sujet traité: "Theoretische Untersuchungen zu optischen Übergängen in Leuchtstoffen am Beispiel ZnO:Cu" (<i>études théoriques des transitions électroniques dans les matériaux luminescents dans le cas ZnO:Cu</i>)
2.11.1992	Obtention du diplôme d'Ingenieur en génie chimique
Depuis Août 1993	Thèse à l'Institut de physique expérimentale de l'Ecole Polytechnique Fédérale de Lausanne (EPFL)

List of Publications

- [1] L. Nedelmann, K. C. Mishra, J. Sticht, and P. C. Schmidt:
“*Theoretical Investigation of the Luminescence Transition Probabilities in the Phosphor ZnO:Cu*”, Berichte der Bunsengesellschaft für Physikalische Chemie **96** (1992) 1765.
- [2] B. Müller, B. Fischer, L. Nedelmann, A. Fricke, and K. Kern:
“*Strain relief on metal interfaces with square symmetry*”, Physical Review Letters **76** (1996) 2358.
- [3] B. Müller, L. Nedelmann, B. Fischer, A. Fricke, and K. Kern:
“*Strain relief in metal heteroepitaxy on face-centered-cubic(100): Cu/Ni(100)*”, Journal of Vacuum Science and Technology A **14** (1996) 1878.
- [4] B. Müller, L. Nedelmann, B. Fischer, H. Brune, and K. Kern:
“*Nucleation and growth of Cu/Ni(100): A variable temperature STM study*”, Surface Reviews and Letters, in press.
- [5] B. Müller, L. Nedelmann, B. Fischer, H. Brune, and K. Kern:
“*Initial stages of Cu epitaxy on Ni(100): Post-nucleation and a well defined transition in critical island size*”, Physical Review B, in press.
- [6] L. Nedelmann, B. Müller, B. Fischer, K. Kern, D. Erdös, and J. Wollschläger:
“*A comparative STM and SPA-LEED study on the evolution of strain induced stripe pattern on Cu/Ni(100)*”, Surface Science, in press.
- [7] B. Müller, L. Nedelmann, B. Fischer, H. Brune, and K. Kern:
“*Submonolayer nucleation and growth of copper on Ni(100)*”, in Surface Diffusion: Atomistic and Collective Processes (M. Scheffler and M. Tringides, eds.), NATO ASI, Series B: Physics (1996) in press.
- [8] B. Müller, L. Nedelmann, B. Fischer, H. Brune, J. V. Barth, and K. Kern:
“*Shape transition from compact to ramified islands in submonolayer heteroepitaxial growth on square lattices*”, submitted.
- [9] B. Fischer, J. V. Barth, A. Fricke, L. Nedelmann, and K. Kern:
“*Growth and surface alloy formation of Al on Au(111)*”, submitted.

*Qu'avais-je besoin de tant d'efforts? Les lignes
douces de ces collines et la main du soir sur ce
coeur agité m'en apprennent bien plus.*

Albert Camus, 'Le mythe de Sisyphe'